

Investigating the theoretical performance of Cs₂TiBr₆-based perovskite solar cell with La-doped BaSnO₃ and CuSbS₂ as the charge transport layers

Kumar Shivesh¹, Intekhab Alam^{2}, A.K. Kushwaha³, Manish Kumar⁴, S.V. Singh¹*

¹Department of Chemical Engineering & Technology, Indian Institute of Technology (Banaras Hindu University), Varanasi, Uttar Pradesh-221005, India

²Department of Mechanical Engineering, Bangladesh University of Engineering and Technology (BUET), East Campus, Dhaka-1000, Bangladesh

³Department of Physics, K.N. Govt. P.G. College, Gyanpur, Bhadohi, Uttar Pradesh-221304, India

⁴Experimental Research Laboratory, Department of Physics, ARSD College, University of Delhi, New Delhi-110021, India

*Corresponding Author

Email: intekhabsanglap@gmail.com, Phone No: +8801819279881

Abstract

A lead-free, completely inorganic, and non-toxic Cs₂TiBr₆-based double perovskite solar cell (PSC) was simulated via SCAPS 1-D. La-doped BaSnO₃ (LBSO) was applied as the electron transport layer (ETL) unprecedentedly in the simulation study of PSCs, while CuSbS₂ was utilized as the hole transport layer (HTL). wxAMPS was used to validate the results of SCAPS simulations. Moreover, the first-principle density function theory (DFT) calculations were performed for validating the 1.6 eV bandgap of the Cs₂TiBr₆ absorber. To enhance the device performance, we analyzed and optimized various parameters of the PSC using SCAPS. The optimum thickness, defect density, and bandgap of the absorber were 1000 nm, 10¹³ cm⁻³, and 1.4 eV, respectively. Furthermore, the optimum thickness, hole mobility, and electron affinity of the HTL were 400 nm, 10² cm²V⁻¹s⁻¹, and 4.1 eV, respectively. However, the ETL thickness had a negligible effect on the device's efficiency. The optimized values of doping density for the absorber layer, HTL, and ETL were 10¹⁵, 10²⁰, and 10²¹ cm⁻³, respectively. Herein, the effect of different HTLs was analyzed by matching up the built-in voltage (V_{bi}) in respect of the open-circuit voltage (V_{oc}). It was found that the V_{bi} was directly proportional to the V_{oc} , and CuSbS₂ was the champion in terms of efficiency for the PSC. The optimum work function of metal contact and temperature of the PSC were 5.9 eV and 300 K, respectively. After the final optimization, the device achieved an exhilarating PCE of 29.13%.

Keywords: La-doped BaSnO₃ electron transport layer, Cs₂TiBr₆ absorber, CuSbS₂ hole transport layer, density function theory calculations, solar cell simulation by SCAPS, solar cell simulation by wxAMPS.

1. Introduction

The halide perovskites (HPs) possess the structure of ABX_3 , where A represents a monovalent cation, B stands for a divalent metal cation, and X denotes a halide anion [1]. These are a group of semiconductor materials with atypical optoelectronic properties, like high absorption coefficient, longer carrier diffusion length, weakly bound exciton, and a wide range of bandgap tunability [2], [3]. However, although these light-harvesting layers surpassed the power conversion efficiency (PCE) in perovskite solar cells (PSCs), there are two leading problems: the toxicity of lead and the PSCs that give high PCE consist of organic cations, like methylammonium and formamidinium ions [4]. These ions are extremely volatile and hygroscopic, thus making the device unstable and more intolerant of heat and moisture [5].

Ti-based $A_2^{+1}Ti^{+4}X_6^{-1}$ double perovskites are lead-free and non-toxic materials that not only can substitute the lead in perovskite but also possess novel optoelectronic applications besides solar cells [6]. According to the density functional theory (DFT) calculations, these HPs have advantageous electronic and optical properties, such as appropriate bandgaps and tuneable defect properties. The processability and stability of these HPs are encouraging their utilization in PSCs [7]. In 2017, Cs_2TiX_6 ($X = F, Cl, Br, \text{ or } I$) was found as an excellent option for an eco-friendly, earth-abundant, and reasonable perovskite light-absorbing layer. The tunability of the bandgap from 1.4 eV to 1.8 eV makes these perovskites fit for the implementation in solar cells [8]. In addition, these HPs have satisfactory electron (L_n) and hole (L_p) diffusion lengths [9]. In the present work, Cs_2TiBr_6 was selected as the absorber layer of the PSC. It exhibits prolonged carrier-diffusion lengths, efficient photoluminescence, as well as energy levels appropriate for the usage in tandem solar cells [6]. Besides, it

demonstrates superior thermal, moisture, and light effects stability than the methylammonium lead iodide (MAPbI₃) thin films, ensuring the higher intrinsic or environmental durability of the Cs₂TiBr₆ thin films [7]. Moreover, Cs₂TiBr₆-based PSC has attained 3.3% efficiency experimentally that is greater than most other double PSCs [7].

The valence band offset (VBO) between the hole transport layer (HTL) and absorber, hole mobility, and cost are the major properties for consideration while selecting an HTL for the PSCs [10]. The researchers mostly use the organic spiro-OMeTAD as the HTL in the PSCs because of its good tunability and processability [2]. However, its poor conductivity, very low hole mobility, high fabrication cost, and environmental instability obstruct its application [11]. Therefore, the inorganic p-type semiconductors are better replacements as the HTL because they possess outstanding chemical stability along with excellent hole mobility [12]. Especially, inorganic Cu-based chalcogenide compounds denoted as Cu_aBX_b, where X = Te, S, or Se and B = Bi, Sn, or Sb, are under investigation for their application in the photovoltaics. The most abundant and cost-effective member of this family is CuSbS₂ [13], [14]. It possesses a direct bandgap of 1.58 eV along with an excellent hole mobility of 49 cm²V⁻¹s⁻¹ [15]. Moreover, its band alignment with Cs₂TiBr₆ perovskite is pretty good for the charge carriers' transfer, thus making it an appropriate HTL for this work.

Although most PSCs use TiO₂ as the electron transport layer (ETL), their stability declines under ultraviolet illumination due to the presence of mesoporous-TiO₂ [16]. To make PSCs more stable, different approaches have been tried, such as fabricating ETL-free PSCs, introducing interfacial layer between perovskite layer and ETL, doping of TiO₂, use of filter UV photocatalytic ability, and insertion of a down-converting layer [17], [18]. Nevertheless, there is another way, which is the replacement of mesoporous-TiO₂ with a new ETL without

deteriorating the PCE of the PSC. BaSnO_3 (BSO), a broad bandgap n-type perovskite oxide, exhibits extensive applications, such as a gas sensor [19], thin-film transistor [20], and transparent conducting oxide [21]. Specifically, La-doped BaSnO_3 expressed as LBSO has high electrical mobility at the ambient temperature [22]. It exhibits lesser ultraviolet photocatalytic ability because of its minimal dipole moment, attributed to the cubic structure without the most frequently occurring distortion in perovskites, i.e., octahedral tilting [23]. In addition, the conduction band offset (CBO) between the LBSO and Cs_2TiBr_6 perovskite is quite low, which makes it a suitable match for this work. The device architecture of the first experimentally fabricated PSC with LBSO as the ETL was FTO/LBSO/ MAPbI_3 /PTAA/Au that had a PCE of 21.3% [23].

In the present work, we reported LBSO as an ETL in the simulation investigations for the first time and designed a fully inorganic and non-toxic FTO/LBSO/ Cs_2TiBr_6 /CuSbS₂/Au heterostructure via SCAPS-1D simulator. We analyzed and optimized the effect of change in thickness, defect density, doping density, and bandgap of the absorber layer, thickness and doping density of ETL along with thickness, doping density, electron affinity, and hole mobility of HTL. We also optimized the operating temperature and metal work function of the PSC. Furthermore, we validated the simulation results using the wxAMPS software. In addition, we also performed theoretical first-principle DFT calculations to validate the bandgap of the Cs_2TiBr_6 perovskite absorber.

2. Methodology

2.1 SCAPS and wxAMPS simulation methodology

The 1-D simulation software SCAPS was used to carry out the numerical study for this work. This C language-based program has been developed by Professor M. Burgelman at the University of Gent, Belgium [24]. This software uses some fundamental semiconductor equations, which are shown in the [Supplementary File](#), to calculate the external quantum efficiency (EQE) curves, current density-voltage (J-V) curves, energy bands, and ac characteristics [3].

We validated our SCAPS simulation results using a 1-D solar simulator software wxAMPS. wxAMPS has been developed at the UIUC, Illinois, United States [2]. Actually, it is an updated version of AMPS developed at the PSU, Pennsylvania, United States [25]. It can generate EQE curves, J-V curves, electrical field distribution, as well as carrier concentration and recombination profiles utilizing some fundamental semiconductor equations [26]. The relevant equations, as well as the comparative results, have been depicted in the [Supplementary File](#) (Table S1 and Fig. S1) [4]. The simulation results of wxAMPS dictated that the values of the photovoltaic properties, namely open-circuit voltage (V_{oc}), fill factor (FF), short-circuit current (J_{sc}), and PCE, were very similar to the values obtained from SCAPS simulation for the PSC. In addition, the SCAPS simulation working procedures are also represented in the [Supplementary File](#) (Fig. S2).

2.2 Device architecture

In this present work, we proposed a device structure of FTO/LBSO/Cs₂TiBr₆/CuSbS₂/Au, as shown in Fig. 1(a). The band energy alignment diagram and band energy diagram of the device have been demonstrated in Fig. 1(b) and Fig. 1(c), respectively. CuSbS₂ was utilized as the p-type inorganic HTL, and Cs₂TiBr₆ was used as the perovskite absorber layer. For the very first time, LBSO was used as the ETL for the numerical simulation study of PSC structure. Fluorine-

doped tin oxide (FTO) and gold (Au) were used as front contact and back contact, respectively.

2.3 Simulated parameters

The data of electrical and optical properties for different layer materials were collected from the previously published experimental and computational research articles. The basic parameters for charge transport layers and absorber layer are tabulated in Table 1. The bulk defect properties of all the layers are listed in Table 2. To make the device closer to reality, we introduced two interfacial defect layers (IDLs) in the PSC. The first one was placed between ETL/perovskite, and another one was inserted between perovskite/HTL [27]. Table 3 shows the interface defect properties of the inserted IDLs. The metal work function (ϕ_{BC}) of Au was taken as 5.1 eV, and 10^7 cm^{-1} was assumed as the thermionic emission/surface recombination velocities for both electrons and holes. All the calculations had been executed at 300 K along with the standard AM1.5G spectrum [28]. The "Eg-sqrt" model had been employed to set the optical absorption constant, $\alpha(h\nu)$, for each layer. The description of this model has been exhibited in the [Supplementary File](#) [2].

2.4 First-principle DFT study of Cs_2TiBr_6

For getting a better insight into the electronic behavior of the studied Cs_2TiBr_6 compound, its electronic band structure and partial density of states (DOS) had been calculated utilizing DFT. The unit cell of the Cs_2TiBr_6 structure was generated via VESTA (a 3D visualization software) and has been shown in Fig. 2(a). All the DFT calculations were done by QUANTUM ESPRESSO distribution [29]. The calculations were done under ultrasoft pseudopotential within the framework of GGA-PBE exchange correlation functional [30], [31]. The kinetic energy cut-offs

for wave functions were used 600 Ry. For the Brillouin zone sampling of electronic states, we used a k-point mesh of 10 x 10 x 10 Monkhorst-Pack [32]. The calculated band structure is illustrated in Fig. 2(b), showing that there was a bandgap of 1.61 eV between the valence band maxima (VBM) and the conduction band minima (CBM). This result was very much comparable with the previously calculated results and the 1.6 eV bandgap of our absorber [9], [33]. We also calculated the partial DOS for the titled compound, and the results are depicted in Fig. 2(c). Fig. 2(c) represents that the valence band between the energy range of -6 eV to -3 eV was mainly constructed by the hybridization of the electrons of 6s-orbitals of Cs-atoms and the 3d-orbitals of Ti-atoms, while the formation of valence band near the Fermi surface was mainly due to the hybridization of 3d-orbitals of Ti-atoms and the 5p-orbitals of Cs-atoms. Besides, the minima of the conduction band had been mainly constructed by the hybridization of 3d-orbitals of Ti-atoms and the 6s-orbitals of Cs-atoms. The higher energy side of the conduction band was mainly constructed by the hybridization of 3d-orbitals of Ti-atoms and the 4p-orbitals of Br-atoms.

3. Results and Discussion

3.1 Effect of the change in absorber layer thickness

In the PSCs, the light-absorbing layer plays a pivotal role in deciding the PCE. In order to find the optimum thickness of the perovskite layer, the thickness of Cs_2TiBr_6 was varied from 700 nm to 2500 nm without changing other parameters. The change in V_{OC} , J_{SC} , FF, and PCE was observed while varying the absorber thickness, and the trends have been illustrated in Fig. 3(a-d).

The V_{OC} increased from 1.0262 V to 1.0274 V with the increasing absorber thickness because the photon-capturing ability of the absorber layer rises with its thickness, which enhances the rate of generation of the charge carriers [27]. Furthermore, the J_{SC} improved from 24.2399 mA/cm² to 25.2551 mA/cm² with the augmentation of absorber thickness. Because there will be a rise of the spectral response at the longer wavelength with the increasing thickness [34]. However, the FF dropped monotonically from 84.70% to 79.03% with the increasing absorber thickness; the deterioration is because of the enhanced series resistance [35]. This can be because of the superiority of carrier recombination along with the presence of parasitic resistance losses [36]. The PCE increased initially with the thickness and reached a maximum value of 21.21% at 1000 nm, which was chosen as the final optimum absorber thickness. Then it declined with a further enhancement in the absorber thickness. The obtained optimum absorber thickness was slightly higher than the 800 nm optimum thickness found for the same absorber material in the published work [37]. The initial rise of PCE can be attributed to an increment in the generation of electron-hole pairs with the increasing thickness. However, the drop of PCE at the higher absorber thickness is due to the enhanced radiative recombination and charge pathway resistance [4].

3.2 Effect of the change in ETL thickness

For designing highly efficient PSCs, the parameters of charge transport layers should be carefully chosen. An appropriate ETL helps in decreasing the recombination currents and increasing the transmittance in PSCs [38]. To find the optimized performance of the PSC, the thickness of LBSO ETL was modulated from 50 nm to 500 nm while maintaining other parameters constant. The effect of ETL thickness on the V_{OC} , J_{SC} , FF, and PCE has been illustrated in Fig. S3(a-d) of the [Supplementary File](#).

The V_{OC} , FF, J_{SC} , and PCE remained almost invariable throughout the variation. The very marginal decrease in J_{SC} and PCE can be due to the partial absorption of light by a thicker ETL, which results in a reduction of the rate of charge generation and collection [39]. The relation between the LBSO thickness and transmittance can be shown by the following equation [40]:

$$\alpha = \frac{1}{d} \ln \frac{1}{T} \dots \dots \dots (1)$$

Where, α is the absorption coefficient, d is the film thickness, and T is the transmittance. It has been reported that the performance loss due to the increasing thickness of ETL gets higher with the reduction in transmittance [39]. It could be concluded from our result that the thickness of LBSO had a negligible effect on PSC performance similar to the published literature [41]. So, 120 nm was taken as the optimum ETL thickness, which was equal to the experimental work [23].

3.3 Effect of the change in HTL thickness

To optimize the thickness of $CuSbS_2$ HTL, the photovoltaic parameters were determined between 100 nm and 1000 nm. The impact of HTL thickness on the V_{OC} , J_{SC} , FF, and PCE has been illustrated in Fig. S4(a-d) of the [Supplementary File](#).

A similar increasing trend of V_{OC} , J_{SC} , and PCE was noticed with the increasing $CuSbS_2$ thickness. The V_{OC} , J_{SC} , and PCE enhanced from 0.9871 V to 1.0506 V, 24.4069 mA/cm² to 25.1296 mA/cm², and 20.55% to 21.67%, respectively. But the FF monotonously reduced from 85.30% to 82.07% as the HTL thickness enhanced. In the previous section, it was observed that the PCE decreased very slightly with the increasing ETL thickness. However, the PCE increased with the increasing HTL thickness similar to the published literature [42]. To minimize the chances of recombination, generally, a p-type layer should be thicker compared

to an n-type layer. Because it helps in transporting an equal number of charge carriers to the terminal immediately [43]. So, the optimum thickness of HTL should be greater than the optimum thickness of ETL, i.e., 120 nm. Therefore, the optimum thickness of HTL was taken 400 nm as the improvement in PCE after that was very marginal. The increased thickness of HTL reinforces the absorption of photons on the light-harvesting layer [43].

3.4 Effect of the change in absorber layer defect density

The absorber defect density (N_t) has a vital influence in deciding the efficiency of PSCs. The PCE of solar cells is greatly influenced by the morphology and quality of the light-absorbing layer. The irradiation of light on the perovskite absorber layer generates photoelectrons. However, poor morphology can cause inadequate coverage of the perovskite layer on the ETL. The inferior quality of film results in higher defect density, which in turn, causes higher recombination [12]. The N_t was modulated from 10^9 cm^{-3} to 10^{16} cm^{-3} for this section. It can be noticed from Fig. 4(a-d) that all of the photovoltaic parameters decreased with the increasing defect density. The V_{OC} , J_{SC} , FF, and PCE significantly reduced from 1.0266 V to 0.8190 V, 24.73 mA/cm^2 to 23.0209 mA/cm^2 , 87.40% to 48.09%, and 22.19% to 9.07%, respectively.

The PSC performance remained almost constant up to 10^{12} cm^{-3} absorber defect density. When the defect density value exceeded 10^{12} cm^{-3} , the performance of the PSC started to decline. This declination can be ascribed to the non-radiative Shockley-Read-Hall (SRH) recombination, which is a principal cause for lifetime reduction, carrier recombination, and a significant reduction in the device performance [2]. The corresponding equations of SRH recombination have been described in the [Supplementary File](#) [4]. To minimize the defect densities, a perovskite with high crystallinity can be an option. The crystallinity can be

improved with the help of pertinent conditions of layer processing [35]. At the lower defect density, the PSC showed higher PCE. But we couldn't take the N_t of 10^9 cm^{-3} as the optimum value at which the PCE was maximum. Because it is not possible to synthesize a material with such a small N_t experimentally [44]. Thus, the optimum defect density of Cs_2TiBr_6 was taken to be 10^{13} cm^{-3} without sacrificing much performance. This optimum absorber N_t was slightly lower than the 10^{14} cm^{-3} optimum N_t attained for the same absorber layer in the published literature [45]. Moreover, the modulation in the total recombination profile of the solar cell with various absorber defect densities has been plotted in Fig. S5 of the [Supplementary File](#).

3.5 Effect of the change in absorber layer doping density

To understand how the acceptor doping concentration (N_A) of the absorber layer affects the photovoltaic parameters, the N_A of the Cs_2TiBr_6 layer was varied from 10^9 cm^{-3} to 10^{19} cm^{-3} . Fig. 5(a-d) illustrates the modulation of V_{OC} , J_{SC} , FF, and PCE with different absorber doping densities. The V_{OC} and J_{SC} improved from 1.0258 V to 1.0267 V and 24.6214 mA/cm^2 to 24.7282 mA/cm^2 , respectively, whereas the FF and PCE dropped from 87.70% to 83.53% and 22.15% to 21.21%, respectively. The PV parameters were constant up to 10^{17} cm^{-3} N_A , which signifies that under the incident of the same number of photons, the generation rate of photo-generated carriers is constant with the absorber doping density.

The Fermi energy level of the hole drops when the absorber doping density increases, which causes the V_{OC} to rise [44]. The built-in potential increases with the increasing N_A of the absorber. This can be another reason behind the increment in V_{OC} because of the elevation of charge separation. Nevertheless, when the N_A value exceeded 10^{17} cm^{-3} , the PCE decreased. As the defect states start to increase at higher N_A , the PCE falls [44]. The optimum N_A lied between 10^9 cm^{-3} and 10^{17} cm^{-3} as the V_{OC} , J_{SC} , FF, and PCE were constant in this range

[46]. The generation of an electric field at the interface layers of the PSC occurs with the increasing absorber doping density. Nevertheless, the occurrence of the recombination of charge carriers is also possible with the generation of the electric field. Therefore, to achieve superior performance, an optimum value of acceptor doping density should be chosen [47]. As the optimum value of N_A should be moderate, it was taken to be 10^{15} cm^{-3} , which was nearly equal to the published research work [12].

3.6 Effect of the change in acceptor doping density of HTL

There are two possible approaches by which the doping of ETL and HTL can be accomplished. It can be achieved with minority carriers, but this approach drastically drops the photovoltaic parameters. Conversely, it can also be accomplished by majority carriers that enormously enhance the PV parameters. An intermediate level of doping density will be helpful for obtaining a better performance of PSCs [34]. To understand the impacts of acceptor doping concentration (N_A) of HTL, the N_A of the CuSbS_2 layer was augmented from 10^{17} cm^{-3} to 10^{21} cm^{-3} [41]. Fig. S6(a) shows the PCE with the varying N_A of HTL, while Fig. S6(b) depicts the J-V curves with different N_A values of HTL in the [Supplementary File](#).

The V_{OC} enhanced from 0.9389 V to 1.1768 V with the increasing N_A of HTL. The increment in the built-in electric potential at the HTL/perovskite interface is the reason behind the higher value of V_{OC} at higher N_A [26]. Besides, the J_{SC} and PCE improved from 24.6859 mA/cm^2 to 24.7464 mA/cm^2 and 19.7% to 21.88%, respectively, with the augmentation of N_A of HTL. The interface electric field among the layers of PSC increases at higher N_A , which brings about the enhancement of electric potential. This reinforces the separation of the charge carriers with reduced recombination speed and enhances the PCE of the PSC [48]. The optimum N_A of CuSbS_2 was taken to be 10^{20} cm^{-3} instead of 10^{21} cm^{-3} at which the maximum PCE was attained. Because a higher value of N_A can create deep coulomb traps, thus declining the hole

mobility [41]. This optimum N_A of HTL was comparable to the previously published literature [49].

3.7 Effect of the change in donor doping density of ETL

Fig. 6(a-d) illustrates the variation of main photovoltaic parameters of the PSC, namely the V_{OC} , J_{SC} , FF, and PCE, against the doping concentration (N_D) of LBSO. To find the optimum doping concentration of ETL, the N_D of LBSO was varied from $1 \times 10^{15} \text{ cm}^{-3}$ to $1 \times 10^{21} \text{ cm}^{-3}$.

The V_{OC} was constant throughout the variation, whereas the J_{SC} narrowly decreased from 24.73 mA/cm^2 to 24.7282 mA/cm^2 by increasing the N_D of ETL. However, the FF and PCE slightly enhanced from 83.22% to 83.53% and 21.13% to 21.21%, respectively, with the increasing N_D , respectively. Because a higher value of the N_D of ETL facilitates charge extraction and charge transport at the ETL/perovskite interface. The performance of the PSC deteriorated at the lower doping density of LBSO, which is attributed to the high series resistance [41], [50]. The optimum N_D of the ETL was taken corresponding to the maximum PCE, i.e., $1 \times 10^{21} \text{ cm}^{-3}$ for the PSC, which was nearly equal to the $2 \times 10^{21} \text{ cm}^{-3}$ N_D of the experimental work [51].

3.8 Effect of the change in absorber bandgap

The energy gap (E_g) of the absorber layer has a major impact on the PCE of the PSC. The bandgap tunability is the most unique property of the perovskites. In this section, the perovskite energy gap was modulated from 1.2 eV to 1.6 eV. Fig. 7(a-d) shows the trends of V_{OC} , J_{SC} , FF, and PCE versus the absorber layer energy gap.

The V_{OC} and FF increased steadily from 0.8549 V to 1.0267 V and 59.80% to 83.53%, respectively, with the increasing absorber bandgap [27]. But there was a drastic decrement

in J_{sc} from 38.0699 mA/cm² to 24.7282 mA/cm² with an increase in the energy gap. Because at a high energy gap, fewer photons get absorbed due to their lower energy compared to the energy gap [41]. There was an increment in PCE from 1.2 eV to 1.4 eV bandgap, achieving a maximum value of 21.87%. However, the PCE started declining after the 1.4 eV bandgap as there is a trade-off. If the bandgap is too high, then an insufficient number of electrons generate due to the very high energy of few photons. In contrast, too low an energy gap enhances the number of electrons but the majority of the energy is dissipated as heat [52]. So, a higher or a lower absorber bandgap with respect to the ideal value of 1.4 eV makes the device inappropriate for solar cell applications due to its declined sunlight absorption capabilities. So, we took 1.4 eV as the optimum absorber bandgap that also exhibited the maximum PCE, similar to the published literature [53].

3.9 Effect of the change in electron affinity of HTL

To enhance the PCE of a PSC, an appropriate energy level alignment between the HTL and perovskite layer is a decisive step. For this reason, the valence band offset ($VBO = E_{V, Absorber} - E_{V, HTL}$) between the HTL and the perovskite layer needs to be analyzed, where E_V is the valence band energy level. Moreover, for balancing among the photovoltaic parameters, the VBO should be less than zero [54]. In this study, the electron affinity (χ_e) of CuSbS₂ was varied from 3.8 eV to 4.3 eV with respect to the perovskite layer for investigating the effect of VBO. The effect of χ_e and E_V of CuSbS₂ on the PSC performance has been shown in Fig. S7 of the [Supplementary File](#).

The observed trends in V_{oc} and PCE with varying χ_e of HTL were almost identical to the published literature [54]. When the VBO was increased from -0.69 eV to -0.39 eV, the V_{oc} and PCE significantly improved from 0.879 V to 1.119 V and 17.11% to 22.4%, respectively. After

-0.39 eV VBO, we observed a drastic reduction in V_{OC} and PCE. Therefore, the optimum VBO for the PSC was taken to be -0.39 eV (corresponding to 4.1 eV χ_e and -5.68 eV E_V of $CuSbS_2$) that gave the maximum PCE. To attenuate the charge recombination at the HTL/perovskite interface, the reduction of VBO is desirable. The deep lowest unoccupied molecule level of HTL with respect to the perovskite layer enables the efficiency improvement of solar cells [54]. After the optimum VBO of -0.39 eV, the PCE dropped that can be because of the creation of the Schottky barrier for the holes. Because of its formation, the propagation of holes to the back contact will be hindered, causing the reduction of the PCE of the PSC [5].

3.10 Optimization of the HTL

In this work, we compared the performance of four different HTLs, namely CuO , Cu_2O , PEDOT:PSS, and P3HT, with the $CuSbS_2$ HTL. It assisted us to find out the most suitable HTL for our proposed PSC. We kept the properties of the ETL and perovskite layer unchanged and simulated for different HTLs. For the sake of proper comparison, we also fixed all the bulk and interface defect parameters the same as the initial device. Moreover, the initial values of thickness, effective density of states, and N_A of $CuSbS_2$ HTL were used for all the HTLs. For the appropriate propagation of electrons from the perovskite to ETL, the CBM of ETL should position below the CBM of the absorber layer. Likewise, for the smooth transfer of holes from the perovskite to HTL, the VBM of HTL should position above that of the perovskite layer. The HTLs were optimized in this study by correlating the V_{OC} to the built-in potential (V_{bi}), where V_{bi} is the difference between the conduction band energy level between the perovskite and ETL interface to the perovskite and HTL interface ($E_{C_PVK/ETL} - E_{C_PVK/HTL}$) divided by the elementary charge (q) [55]. The basic parameters for the alternative HTLs are tabulated in Table 4. Besides, the simulated parameters for various HTLs have been tabulated in Table 5.

Fig. 8(a-b) shows the photovoltaic parameters, whereas Fig. 9(a) and Fig. 9(b) illustrate J-V and QE curves, respectively. Fig. 1(b), as well as Fig. S8(a-d) of the [Supplementary File](#), display the energy band alignment diagrams. Furthermore, Fig. 1(c), as well as Fig. S9(a-d) of the [Supplementary File](#), display the energy band diagrams.

From Table 5, it was apparent that the V_{bi} was directly proportional to the V_{OC} similar to the published work [55]. The lowest PCE of 12.82% was shown by P3HT HTL because of the $E_{C_ETL} - E_{V_HTL} = 0.55$ eV, which exhibited the least qV_{bi} of 0.29 eV and thus dropped the V_{OC} to 0.729 V. Moreover, P3HT had the lowest charge carrier mobility among the investigated HTLs, and its conductivity showed non-linear characteristics with respect to the doping concentration [55]. Because of these reasons, the P3HT HTL had the worst performance among all the HTLs. However, the $CuSbS_2$ HTL gained the highest qV_{bi} , i.e., 0.91 eV, which increased the V_{OC} to 1.0267 V. It was the primary reason for the highest PCE of 21.21% achieved by the $CuSbS_2$ HTL. Furthermore, $CuSbS_2$ had a good charge carrier mobility and superior band alignment with the perovskite layer and metal contact. Hence, the primarily used $CuSbS_2$ was considered as the best HTL for the PSC. Moreover, there was not much variation in the QE curves for different HTLs. Because the optical absorption coefficient of the HTL is insignificant as it is positioned at the rear end of the device [56].

3.11 Effect of the change in back contact work function

The creation of an ohmic contact is mandatory for facilitating the appropriate collection of holes through the back contact [55]. In our previous simulations, Au was employed as the back contact with a work function (ϕ_{BC}) of 5.1 eV. Different ϕ_{BC} values were analyzed in this section to understand their effect on the PSC. Fig. 10(a-d) illustrates the effect of ϕ_{BC} on the V_{OC} , J_{SC} , FF, and PCE, while the ϕ_{BC} was tuned from 4.9 eV to 6.0 eV. Fig. 11(a) illustrates that

when the ϕ_{BC} was 4.9 eV, a Schottky barrier was present in the energy band diagram, whereas there was no barrier when the ϕ_{BC} was 6.0 eV according to Fig. 11(b). A Schottky barrier for holes can be generated when the work function becomes equal to the VBM of HTL or lower than the VBM of HTL as depicted in Fig. 11(a). But the Schottky barrier can vanish at a higher value of ϕ_{BC} as the ϕ_{BC} matches with the Fermi level of HTL as shown in Fig. 11(b), which results in the improvement of PCE.

The observed trends in V_{OC} , J_{SC} , FF, and PCE with varying ϕ_{BC} were similar to the published literature [57]. The V_{OC} and J_{SC} enhanced from 0.8267 to 1.2194 V and 24.727 to 25.0959 mA/cm², respectively, with the increasing ϕ_{BC} . When the ϕ_{BC} is low, the V_{OC} falls because of the declination in the built-in voltage of the PSC. At the same time, the J_{SC} decreases because of the inadequate collection of electron-hole pairs [2]. Moreover, with the increasing ϕ_{BC} , the FF increased to a maximum value of 86.21%, and then, it declined. The variation in FF may be attributed to the alteration in the reverse saturation current [57]. The PCE showed an upward trend with the increasing ϕ_{BC} , attaining a maximum value of 25.69% at 5.9 eV. But the PCE remained invariable after 5.9 eV, which was taken as the optimum ϕ_{BC} . Therefore, Se, with a ϕ_{BC} of 5.9 eV, can be a probable substitution of Au to enhance the device performance. As the Schottky barrier diminishes at the higher ϕ_{BC} that causes a reduction in the series resistance, the PCE improves. However, the ohmic resistance increases at the interface HTL/back contact with the increasing ϕ_{BC} , and consequently, the performance gets saturated [47].

3.12 Effect of the change in temperature

As the solar cells are usually set up in outdoor conditions, they face constant illumination from the sun. So, their temperature can become quite high compared to room temperature [58]. So, it is essential to figure out the impact of temperature on the PV parameters of PSCs.

Herein, the operating temperature was modulated from 300 K to 540 K. Fig. S10(a-d) of the [Supplementary File](#) shows the photovoltaic parameters trends against the operating temperature. The V_{oc} attenuated from 1.0267 V to 0.7392 V because of the increment in reverse saturation current density (J_0) at the higher temperature, and the inverse relationship between the V_{oc} and J_0 . The correlation between them can be observed in equation (2):

$$V_{oc} = \frac{AK_B T}{q} \left[\ln \left(1 + \frac{J_{sc}}{J_0} \right) \right] \dots \dots \dots (2)$$

Here, A stands for the ideality factor, and $K_B T/q$ represents the thermal voltage. Moreover, the defects enhance with the increasing temperature, which in turn, decrease the V_{oc} [4].

For the PSC, there was hardly any change that could be noticed for J_{sc} . But at the higher temperature, the values of FF and PCE deteriorated drastically from 83.53% to 72.72% and 21.21% to 13.30%, respectively, which can be due to the reduction in shunt resistance [58].

In addition, the resistance in charge transfer rises with the temperature, thus deteriorating the charge recombination resistance and enhancing the recombination of charge carriers. Moreover, the other reasons for the deterioration of PCE with the augmentation of temperature can be the increment of ohmic resistance at the interfaces of different layers and the declination of the interfacial photo-carrier extraction in the PSC. To facilitate the PCE of PSC, additives can be introduced in HTL while performing fabrication [47]. The simulation result depicts that the PCE was highest at the room temperature of 300 K, which was taken as the optimum temperature for the PSC. This optimum temperature was comparable to the previously published works [4], [47].

3.13 Effect of the change in HTL hole mobility

According to the definition, the hole mobility (μ_h) represents how a hole propagates under an electric field. The μ_h of an HTL is influenced by its N_A and doping level. At a high acceptor doping level, the ionized impurity scattering limits the μ_h . But at a low acceptor doping level, the lattice scattering limits the μ_h [2]. To scrutinize the impact of the μ_h of CuSbS_2 on the PV parameters, the μ_h was varied from $10^{-4} \text{ cm}^2\text{V}^{-1}\text{s}^{-1}$ to $10^2 \text{ cm}^2\text{V}^{-1}\text{s}^{-1}$. Fig. S11(a) shows the PCE trends against the μ_h of CuSbS_2 , whereas Fig. S11(b) depicts the J-V curves with different hole mobilities in the [Supplementary File](#).

As the μ_h of CuSbS_2 was augmented, the J_{SC} remained almost invariable, whereas the V_{OC} augmented drastically from 0.6854 V to 1.0317 V [59]. The PCE significantly improved from 12.65% to 21.33% by enhancing the μ_h of CuSbS_2 because of the upgradation of hole conduction via the p-type layer. As the CuSbS_2 layer has elevated N_A and μ_h , its presence facilitates the PCE of the PSC [35]. Furthermore, a low μ_h is a reason behind the high series resistance, which in turn, causes deterioration in PCE [43]. The μ_h of the CuSbS_2 ($10^2 \text{ cm}^2\text{V}^{-1}\text{s}^{-1}$) corresponding to the maximum PCE was taken as the optimum value.

The finally optimized J-V and QE curves have been shown in Fig. 12(a) and Fig. 12(b), respectively. After the final optimization, the device achieved a V_{OC} of 1.1106 eV, J_{SC} of 29.60 mA/cm^2 , FF of 88.58%, and PCE of 29.13%. Therefore, the PCE of the device significantly improved by 7.92% in magnitude from the initial value of 21.21%. Table 6 depicts the comparison of the optimized device with the previous computational and experimental works on Cs_2TiBr_6 and MAPbI_3 -based PSCs. Unlike MAPbI_3 , Cs_2TiBr_6 has been infrequently studied as the absorber layer. It can be seen from Table 6 that our optimized device's performance was the best among all other existing PSCs. The absence of Pb made our device eco-friendly, and the use of all inorganic charge transport layers enforced its stability in the environment.

4. Conclusion

In this paper, we carried out a simulation study of an environmentally benign, non-toxic, and fully inorganic Cs_2TiBr_6 -based PSC. Lead-free Cs_2TiBr_6 double perovskite was employed as the absorber layer. Moreover, for the very first time, LBSO was explored as the ETL for the simulation investigations of the PSC structure, replacing the commonly used TiO_2 . To facilitate charge transportation, inorganic CuSbS_2 was used as the HTL instead of the traditionally used organic spiro-OMeTAD. The first-principle DFT calculations were performed to validate the 1.6 eV bandgap of the Cs_2TiBr_6 perovskite. In addition, we scrutinized the impact of various modulators on the PSC's PV parameters via SCAPS 1-D. The PSC showed the highest PCE at 1000 nm absorber thickness. However, we did not find any significant changes in PCE while modulating the thickness of LBSO. We finalized 400 nm thick CuSbS_2 as the optimal HTL, and the optimum absorber defect density was chosen as 10^{13} cm^{-3} . The optimized values of the doping density for the Cs_2TiBr_6 , CuSbS_2 , and LBSO were found to be 10^{15} , 10^{20} , and 10^{21} cm^{-3} , respectively. Besides, the highest PCE occurred at the 1.4 eV absorber bandgap. The effect of VBO between the HTL and the absorber was investigated by changing the κ_e of CuSbS_2 , and the simulation results showed the maximum PCE at 4.1 eV κ_e . Furthermore, different HTLs were investigated for the PSC by matching up the V_{bi} with the V_{OC} . The V_{bi} was found directly proportional to the V_{OC} , and the originally used CuSbS_2 showed the best PCE among all the HTLs. The optimum ϕ_{BC} was selected as 5.9 eV for the PSC, suggesting that Se can be a good replacement for Au as the back contact. Moreover, we identified that the PCE decreased with the increasing temperature, while it enhanced with the augmentation of the μ_h of HTL. Finally, the fully optimized device attained a PCE of 29.13%, which was a drastic improvement over the initial PCE of 21.21%. In addition, the validation of the SCAPS simulation was accomplished

via wxAMPS. Therefore, the numerical simulation study of this proposed device will deliver a perspective for the development of a highly efficient, eco-friendly, and lead-free PSC.

Acknowledgment

The authors would like to thank Dr. M. Burgelman at the University of Gent, Belgium, for issuing the SCAPS-1D software. They also would like to acknowledge Prof. A. Rockett and Dr. Yiming Liu from UIUC and Prof. Fonash of PSU for delivering the wxAMPS software.

References

- [1] M. Saliba *et al.*, "Cesium-containing triple cation perovskite solar cells: Improved stability, reproducibility and high efficiency," *Energy Environ. Sci.*, vol. 9, no. 6, pp. 1989–1997, 2016, doi: 10.1039/c5ee03874j.
- [2] I. Alam, R. Mollick, and M. A. Ashraf, "Numerical simulation of Cs₂AgBiBr₆-based perovskite solar cell with ZnO nanorod and P3HT as the charge transport layers," *Phys. B Condens. Matter*, vol. 618, p. 413187, 2021, doi: 10.1016/j.physb.2021.413187.
- [3] M. Kumar, A. Kumar, A. Raj, P. C. Sati, M. Sahni, and A. Anshul, "Organic-inorganic perovskite-based solar cell designs for high conversion efficiency: A comparative study by SCAPS simulation," *Mater. Today Proc.*, 2020, doi: 10.1016/j.matpr.2020.11.035.
- [4] I. Alam and M. A. Ashraf, "Effect of different device parameters on tin-based perovskite solar cell coupled with In₂S₃ electron transport layer and CuSCN and Spiro-OMeTAD alternative hole transport layers for high-efficiency performance," *Energy Sources, Part A Recover. Util. Environ. Eff.*, vol. 2020, 2020, doi: 10.1080/15567036.2020.1820628.
- [5] Y. Raoui, H. Ez-Zahraouy, S. Ahmad, and S. Kazim, "Unravelling the theoretical window to fabricate high performance inorganic perovskite solar cells," *Sustain. Energy Fuels*, vol. 5, no. 1, pp. 219–229, 2021, doi: 10.1039/d0se01160f.
- [6] G. K. Grandhi *et al.*, "Lead-free cesium titanium bromide double perovskite nanocrystals," *Nanomaterials*, vol. 11, no. 6, 2021, doi: 10.3390/nano11061458.
- [7] M. Chen *et al.*, "Cesium Titanium(IV) Bromide Thin Films Based Stable Lead-free Perovskite Solar Cells," *Joule*, vol. 2, no. 3, pp. 558–570, 2018, doi: 10.1016/j.joule.2018.01.009.
- [8] M. G. Ju *et al.*, "Earth-Abundant Nontoxic Titanium(IV)-based Vacancy-Ordered Double Perovskite Halides with Tunable 1.0 to 1.8 eV Bandgaps for Photovoltaic Applications," *ACS Energy Lett.*, vol. 3, no. 2, pp. 297–304, 2018, doi: 10.1021/acseenergylett.7b01167.
- [9] K. Chakraborty, M. G. Choudhury, and S. Paul, "Numerical study of Cs₂TiX₆ (X = Br⁻, I⁻, F⁻ and Cl⁻) based perovskite solar cell using SCAPS-1D device simulation," *Sol. Energy*, vol. 194, pp. 886–892, 2019, doi: 10.1016/j.solener.2019.11.005.
- [10] N. Singh, A. Agarwal, and M. Agarwal, "Performance evaluation of lead-free double-perovskite solar cell," *Opt. Mater. (Amst.)*, vol. 114, p. 110964, 2021, doi: 10.1016/j.optmat.2021.110964.
- [11] H. Choi, S. Park, S. Paek, P. Ekanayake, M. K. Nazeeruddin, and J. Ko, "Efficient star-shaped hole transporting materials with diphenylethenyl side arms for an efficient perovskite solar cell," *J. Mater. Chem. A*, vol. 2, no. 45, pp. 19136–19140, 2014, doi: 10.1039/C4TA04179H.
- [12] S. Z. Haider, H. Anwar, and M. Wang, "Theoretical Device Engineering for High-Performance Perovskite Solar Cells Using CuSCN as Hole Transport Material Boost the Efficiency Above 25%," *Phys. Status Solidi Appl. Mater. Sci.*, vol. 216, no. 11, pp. 1–12, 2019, doi: 10.1002/pssa.201900102.
- [13] C. Garza *et al.*, "p-Type CuSbS₂ thin films by thermal diffusion of copper into Sb₂S₃," *Sol. Energy Mater. Sol. Cells*,

- vol. 95, no. 8, pp. 2001–2005, 2011, doi: 10.1016/J.SOLMAT.2010.06.011.
- [14] J. van Embden and Y. Tachibana, “Synthesis and characterisation of famatinite copper antimony sulfide nanocrystals,” *J. Mater. Chem.*, vol. 22, no. 23, pp. 11466–11469, May 2012, doi: 10.1039/C2JM32094K.
- [15] C. Devi and R. Mehra, “Device simulation of lead-free MASnI₃ solar cell with CuSbS₂ (copper antimony sulfide),” *J. Mater. Sci.*, vol. 54, no. 7, pp. 5615–5624, 2019, doi: 10.1007/s10853-018-03265-y.
- [16] M. Liu, M. B. Johnston, and H. J. Snaith, “Efficient planar heterojunction perovskite solar cells by vapour deposition,” *Nature*, vol. 501, no. 7467, pp. 395–398, 2013, doi: 10.1038/nature12509.
- [17] W. Li *et al.*, “Enhanced UV-light stability of planar heterojunction perovskite solar cells with caesium bromide interface modification,” *Energy Environ. Sci.*, vol. 9, no. 2, pp. 490–498, 2016, doi: 10.1039/c5ee03522h.
- [18] T. Leijtens, G. E. Eperon, S. Pathak, A. Abate, M. M. Lee, and H. J. Snaith, “Overcoming ultraviolet light instability of sensitized TiO₂ with meso-superstructured organometal tri-halide perovskite solar cells,” *Nat. Commun.*, vol. 4, pp. 1–8, 2013, doi: 10.1038/ncomms3885.
- [19] J. Cerdà, J. Arbiol, G. Dezanneau, R. Díaz, and J. R. Morante, “Perovskite-type BaSnO₃ powders for high temperature gas sensor applications,” *Sensors Actuators, B Chem.*, vol. 84, no. 1, pp. 21–25, 2002, doi: 10.1016/S0925-4005(02)00005-9.
- [20] Y. M. Kim, C. Park, U. Kim, C. Ju, and K. Char, “High-mobility BaSnO₃ thin-film transistor with HfO₂ gate insulator,” *Appl. Phys. Express*, vol. 9, no. 1, p. 011201, 2015, doi: 10.7567/APEX.9.011201.
- [21] D. O. Scanlon, “Defect engineering of BaSnO₃ for high-performance transparent conducting oxide applications,” *Phys. Rev. B - Condens. Matter Mater. Phys.*, vol. 87, no. 16, pp. 1–5, 2013, doi: 10.1103/PhysRevB.87.161201.
- [22] H. J. Kim *et al.*, “High mobility in a stable transparent perovskite oxide,” *Appl. Phys. Express*, vol. 5, no. 6, pp. 8–11, 2012, doi: 10.1143/APEX.5.061102.
- [23] S. S. Shin *et al.*, “Colloidally prepared La-doped BaSnO₃ electrodes for efficient, photostable perovskite solar cells,” *Science (80-.)*, vol. 356, no. 6334, pp. 167–171, 2017, doi: 10.1126/science.aam6620.
- [24] A. Niemegeers and M. Burgelman, “Numerical modelling of ac-characteristics of CdTe and CIS solar cells,” *Conf. Rec. IEEE Photovolt. Spec. Conf.*, pp. 901–904, 1996, doi: 10.1109/pvsc.1996.564274.
- [25] J. Gong and S. Krishnan, “Simulation of inverted perovskite solar cells,” *ASME 2018 12th Int. Conf. Energy Sustain. ES 2018, collocated with ASME 2018 Power Conf. ASME 2018 Nucl. Forum*, pp. 1–7, 2018, doi: 10.1115/es2018-7227.
- [26] Y. Cao *et al.*, “Towards high efficiency inverted Sb₂Se₃ thin film solar cells,” *Sol. Energy Mater. Sol. Cells*, vol. 200, 2019, doi: 10.1016/j.solmat.2019.109945.
- [27] S. Rai, B. K. Pandey, and D. K. Dwivedi, “Designing hole conductor free tin–lead halide based all-perovskite heterojunction solar cell by numerical simulation,” *J. Phys. Chem. Solids*, vol. 156, p. 110168, 2021, doi: 10.1016/j.jpcs.2021.110168.
- [28] S. Abdelaziz, A. Zekry, A. Shaker, and M. Abouelatta, “Investigating the performance of formamidinium tin-based perovskite solar cell by SCAPS device simulation,” *Opt. Mater. (Amst.)*, vol. 101, p. 109738, 2020, doi: 10.1016/j.optmat.2020.109738.
- [29] P. Giannozzi *et al.*, “QUANTUM ESPRESSO: A modular and open-source software project for quantum simulations of materials,” *J. Phys. Condens. Matter*, vol. 21, no. 39, 2009, doi: 10.1088/0953-8984/21/39/395502.
- [30] J. P. Perdew, K. Burke, and M. Ernzerhof, “Generalized gradient approximation made simple,” *Phys. Rev. Lett.*, vol. 77, no. 18, pp. 3865–3868, 1996, doi: 10.1103/PhysRevLett.77.3865.
- [31] J. P. Perdew *et al.*, “Restoring the density-gradient expansion for exchange in solids and surfaces,” *Phys. Rev. Lett.*, vol. 100, no. 13, pp. 1–4, 2008, doi: 10.1103/PhysRevLett.100.136406.
- [32] H. J. Monkhorst and J. D. Pack, “Special points for Brillouin-zone integrations,” *Phys. Rev. B*, vol. 13, no. 12, p. 5188, Jun. 1976, doi: 10.1103/PhysRevB.13.5188.
- [33] D. Liu *et al.*, “The effects of cation and halide anion on the electronic and optical properties of Ti-based double perovskite: A first-principles calculations,” *J. Phys. Chem. Solids*, vol. 150, p. 109852, 2021, doi: 10.1016/j.jpcs.2020.109852.
- [34] U. Mandadapu, “Simulation and Analysis of Lead based Perovskite Solar Cell using SCAPS-1D,” *Indian J. Sci. Technol.*, vol. 10, no. 1, pp. 1–8, 2017, doi: 10.17485/ijst/2017/v11i10/110721.

- [35] L. Lin, L. Jiang, P. Li, B. Fan, and Y. Qiu, "A modeled perovskite solar cell structure with a Cu₂O hole-transporting layer enabling over 20% efficiency by low-cost low-temperature processing," *J. Phys. Chem. Solids*, vol. 124, pp. 205–211, 2019, doi: 10.1016/j.jpcs.2018.09.024.
- [36] M. Kumar, A. Raj, A. Kumar, and A. Anshul, "Theoretical evidence of high power conversion efficiency in double perovskite solar cell device," *Opt. Mater. (Amst.)*, vol. 111, pp. 17–18, 2021, doi: 10.1016/j.optmat.2020.110565.
- [37] M. R. Jani *et al.*, "Exploring solar cell performance of inorganic Cs₂TiBr₆ halide double perovskite: A numerical study," *Superlattices Microstruct.*, vol. 146, p. 106652, 2020, doi: 10.1016/j.spmi.2020.106652.
- [38] A. Tara, V. Bharti, S. Sharma, and R. Gupta, "Device simulation of FASnI₃ based perovskite solar cell with Zn(O_{0.3}, S_{0.7}) as electron transport layer using SCAPS-1D," *Opt. Mater. (Amst.)*, vol. 119, p. 111362, 2021, doi: 10.1016/j.optmat.2021.111362.
- [39] Y. Raoui, H. Ez-Zahraouy, N. Tahiri, O. El Bounagui, S. Ahmad, and S. Kazim, "Performance analysis of MAPbI₃ based perovskite solar cells employing diverse charge selective contacts: Simulation study," *Sol. Energy*, vol. 193, pp. 948–955, 2019, doi: 10.1016/j.solener.2019.10.009.
- [40] A. Kumar, S. Maurya, S. Patwardhan, and K. R. Balasubramaniam, "Opto-electronic properties of poly-crystalline Ia doped BaSnO₃ films deposited on quartz substrates," *J. Phys. D. Appl. Phys.*, vol. 54, no. 18, 2021, doi: 10.1088/1361-6463/abe271.
- [41] M. M. Salah, M. Abouelatta, A. Shaker, K. M. Hassan, and A. Saeed, "A comprehensive simulation study of hybrid halide perovskite solar cell with copper oxide as HTM," *Semicond. Sci. Technol.*, vol. 34, no. 11, p. 115009, 2019, doi: 10.1088/1361-6641/ab22e1.
- [42] J. Adeyemi Owolabi, M. Yusuf Onimisi, J. Amuchi Ukwanya, A. Bulus Bature, and U. Raphael Ushiekpan, "Investigating the Effect of ZnSe (ETM) and Cu₂O (HTM) on Absorber Layer on the Performance of Pervoskite Solar Cell Using SCAPS-1D," *Am. J. Phys. Appl.*, vol. 8, no. 1, p. 8-18, 2020, doi: 10.11648/j.ajpa.20200801.12.
- [43] O. Ahmad, A. Rashid, M. W. Ahmed, M. F. Nasir, and I. Qasim, "Performance evaluation of Au/p-CdTe/Cs₂TiI₆/n-TiO₂/ITO solar cell using SCAPS-1D," *Opt. Mater. (Amst.)*, vol. 117, p. 111105, 2021, doi: 10.1016/j.optmat.2021.111105.
- [44] P. K. Patel, "Device simulation of highly efficient eco-friendly CH₃NH₃SnI₃ perovskite solar cell," *Sci. Rep.*, vol. 11, no. 1, pp. 1–11, 2021, doi: 10.1038/s41598-021-82817-w.
- [45] M. A. K. Khan, S. S. Urmi, T. T. Ferdous, S. Azam, and M. A. Alim, "Highly efficient Cesium Titanium (IV) Bromide perovskite solar cell and its point defect investigation: A computational study," *Superlattices Microstruct.*, vol. 156, p. 106946, 2021, doi: 10.1016/j.spmi.2021.106946.
- [46] D. Eli *et al.*, "Simulation and optimization of lead-based perovskite solar cells with cuprous oxide as a P-type inorganic layer," *J. Niger. Soc. Phys. Sci.*, vol. 1, no. 2, pp. 72–81, 2019, doi: 10.46481/jnsps.2019.13.
- [47] K. D. Jayan and V. Sebastian, "Comparative performance analysis of mixed halide perovskite solar cells with different transport layers and back metal contacts," *Semicond. Sci. Technol.*, vol. 36, no. 6, 2021, doi: 10.1088/1361-6641/abf46c.
- [48] A. Mohandes, M. Moradi, and H. Nadgaran, "Numerical simulation of inorganic Cs₂AgBiBr₆ as a lead-free perovskite using device simulation SCAPS-1D," *Opt. Quantum Electron.*, vol. 53, no. 6, pp. 1–22, 2021, doi: 10.1007/s11082-021-02959-z.
- [49] S. A. Moiz, A. N. M. Alahmadi, and A. J. Aljohani, "Design of a Novel Lead-Free Perovskite Solar Cell for 17.83% Efficiency," *IEEE Access*, vol. 9, pp. 54254–54263, 2021, doi: 10.1109/ACCESS.2021.3070112.
- [50] A. Mohandes, M. Moradi, and H. Nadgaran, "Numerical simulation of inorganic Cs₂AgBiBr₆ as a lead-free perovskite using device simulation SCAPS-1D," vol. 6, pp. 1–22, 2021.
- [51] H. F. Wang, Q. Z. Liu, F. Chen, G. Y. Gao, W. Wu, and X. H. Chen, "Transparent and conductive oxide films with the perovskite structure: La- and Sb-doped BaSnO₃," *J. Appl. Phys.*, vol. 101, no. 10, pp. 88–91, 2007, doi: 10.1063/1.2736629.
- [52] Sadanand and D. K. Dwivedi, "Modeling of photovoltaic solar cell based on CuSbS absorber for the enhancement of performance," *IEEE Trans. Electron Devices*, vol. 68, no. 3, pp. 1121–1128, 2021, doi: 10.1109/TED.2020.3048326.
- [53] M. Kumar, A. Raj, A. Kumar, and A. Anshul, "Effect of band-gap tuning on lead-free double perovskite heterostructure devices for photovoltaic applications via SCAPS simulation," *Mater. Today Commun.*, vol. 26, pp. 8–12, 2021, doi: 10.1016/j.mtcomm.2020.101851.

- [54] Y. Raoui, H. Ez-Zahraouy, S. Kazim, and S. Ahmad, "Energy level engineering of charge selective contact and halide perovskite by modulating band offset: Mechanistic insights," *J. Energy Chem.*, vol. 54, pp. 822–829, 2021, doi: 10.1016/j.jechem.2020.06.030.
- [55] N. Singh, A. Agarwal, and M. Agarwal, "Numerical simulation of highly efficient lead-free all-perovskite tandem solar cell," *Sol. Energy*, vol. 208, pp. 399–410, 2020, doi: 10.1016/j.solener.2020.08.003.
- [56] M. B. Kanoun, A. A. Kanoun, A. E. Merad, and S. Goumri-Said, "Device design optimization with interface engineering for highly efficient mixed cations and halides perovskite solar cells," *Results Phys.*, vol. 20, p. 103707, 2021, doi: 10.1016/j.rinp.2020.103707.
- [57] K. Deepthi Jayan and V. Sebastian, "Comprehensive device modelling and performance analysis of MASnI₃ based perovskite solar cells with diverse ETM, HTM and back metal contacts," *Sol. Energy*, vol. 217, pp. 40–48, 2021, doi: 10.1016/j.solener.2021.01.058.
- [58] N. Singh, A. Agarwal, and M. Agarwal, "Numerical simulation of highly efficient lead-free perovskite layers for the application of all-perovskite multi-junction solar cell," *Superlattices Microstruct.*, vol. 149, p. 106750, 2021, doi: 10.1016/j.spmi.2020.106750.
- [59] F. Liu *et al.*, "Numerical simulation: Toward the design of high-efficiency planar perovskite solar cells," *Appl. Phys. Lett.*, vol. 104, no. 25, 2014, doi: 10.1063/1.4885367.
- [60] B. Hadjarab, A. Bouguelia, and M. Trari, "Optical and transport properties of lanthanum-doped stannate BaSnO₃," *J. Phys. D: Appl. Phys.*, vol. 40, no. 19, pp. 5833–5839, 2007, doi: 10.1088/0022-3727/40/19/006.
- [61] Y. Guo, Y. Xue, C. Geng, C. Li, X. Li, and Y. Niu, "Structural, Electronic, and Optical Characterizations of the Interface between CH₃NH₃PbI₃ and BaSnO₃ Perovskite: A First-Principles Study," *J. Phys. Chem. C*, vol. 123, no. 26, pp. 16075–16082, 2019, doi: 10.1021/acs.jpcc.9b01088.
- [62] S. Ahmed, F. Jannat, and M. A. Alim, "A study of Cesium Titanium Bromide based perovskite solar cell with different Hole and Electron transport materials," *2020 2nd Int. Conf. Adv. Inf. Commun. Technol. ICAICT 2020*, no. November 2020, pp. 297–301, 2020, doi: 10.1109/ICAICT51780.2020.9333520.
- [63] D. Jayan K. and V. Sebastian, "Comparative Study on the Performance of Different Lead-Based and Lead-Free Perovskite Solar Cells," *Adv. Theory Simulations*, vol. 4, no. 5, May 2021, doi: 10.1002/adts.202100027.
- [64] M. Shasti and A. Mortezaali, "Numerical Study of Cu₂O, SrCu₂O₂, and CuAlO₂ as Hole-Transport Materials for Application in Perovskite Solar Cells," *Phys. Status Solidi Appl. Mater. Sci.*, vol. 216, no. 18, pp. 1–10, 2019, doi: 10.1002/pssa.201900337.
- [65] M. Samanta, S. I. Ahmed, K. K. Chattopadhyay, and C. Bose, "Role of various transport layer and electrode materials in enhancing performance of stable environment-friendly Cs₂TiBr₆ solar cell," *Optik (Stuttg.)*, vol. 217, p. 164805, 2020, doi: 10.1016/j.ijleo.2020.164805.
- [66] S. Ahmed, F. Jannat, M. A. K. Khan, and M. A. Alim, "Numerical development of eco-friendly Cs₂TiBr₆ based perovskite solar cell with all-inorganic charge transport materials via SCAPS-1D," *Optik (Stuttg.)*, vol. 225, p. 165765, 2021, doi: 10.1016/j.ijleo.2020.165765.
- [67] S. K. Meza and N. K. Hassan, "Cs₂TiBr₆ Solar Cell Performance Enhancement by Different Absorber Layer Thickness," vol. 15, no. 1, pp. 33–36, 2021.

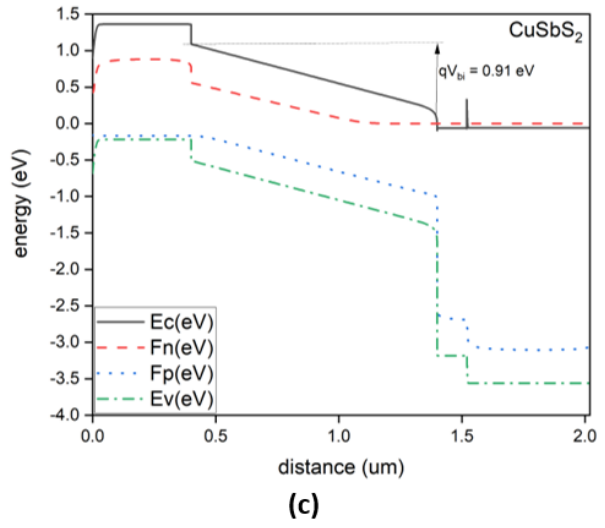
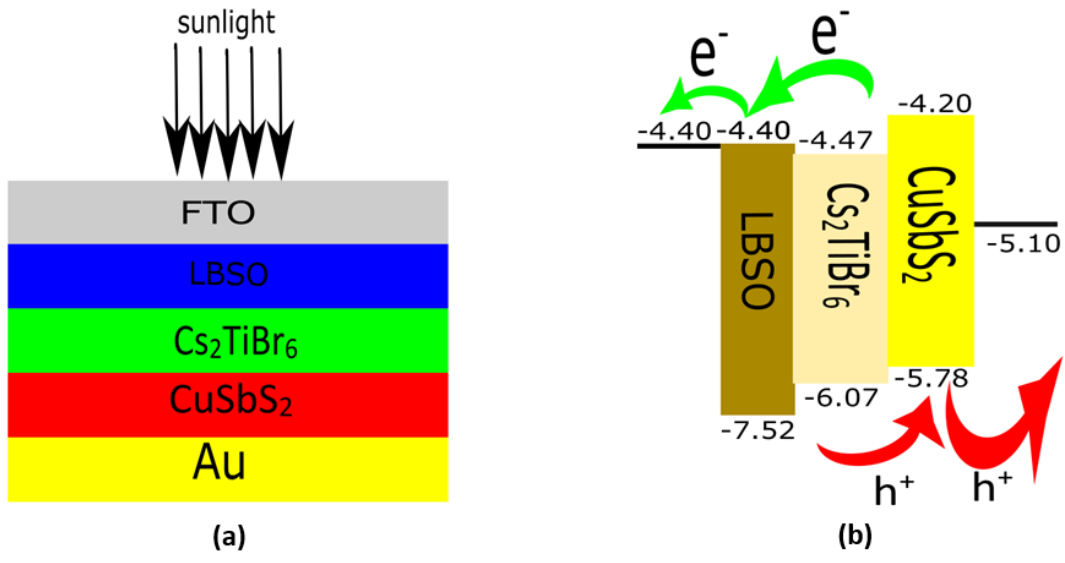
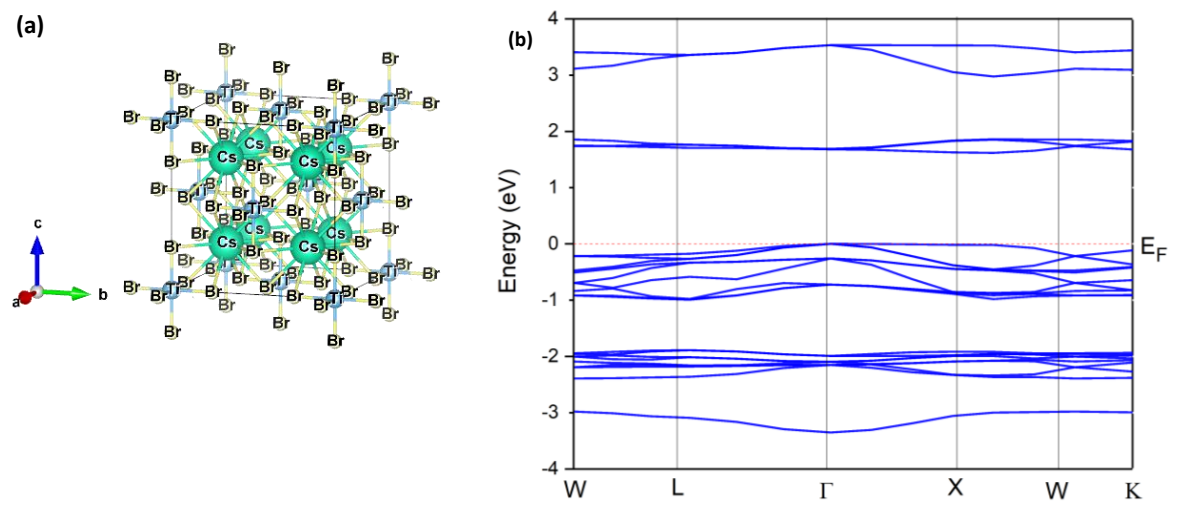


Fig. 1. (a) Schematic diagram, (b) Energy band alignment diagram, and (c) Energy band diagram of FTO/LBSO/ Cs_2TiBr_6 / CuSbS_2 /Au.



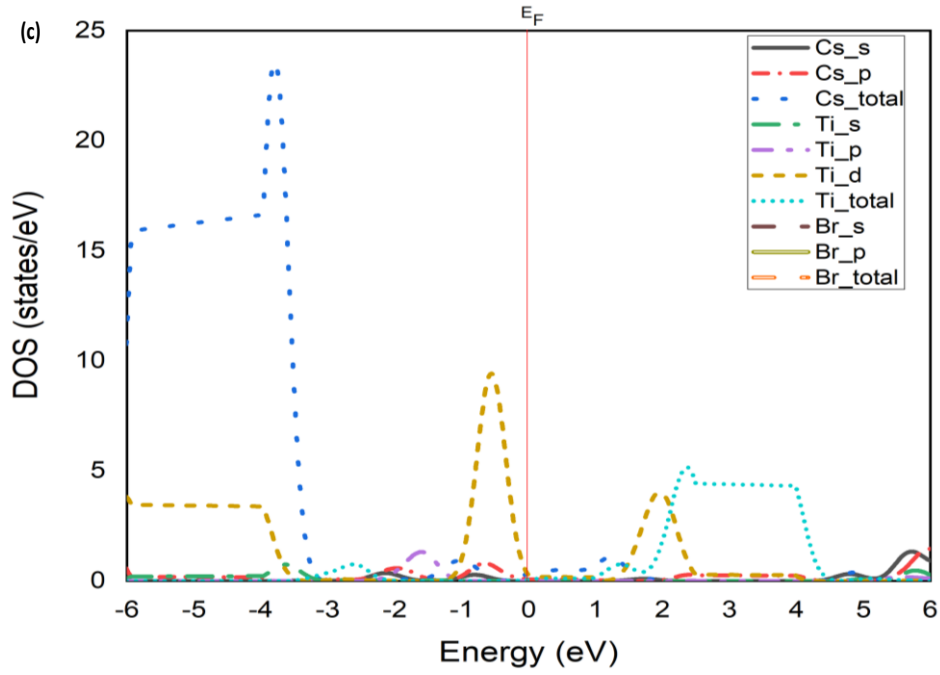


Fig. 2. (a) Unit cell of Cs_2TiBr_6 structure, (b) Band structure profile of Cs_2TiBr_6 , and (c) DOS profile of Cs_2TiBr_6 .

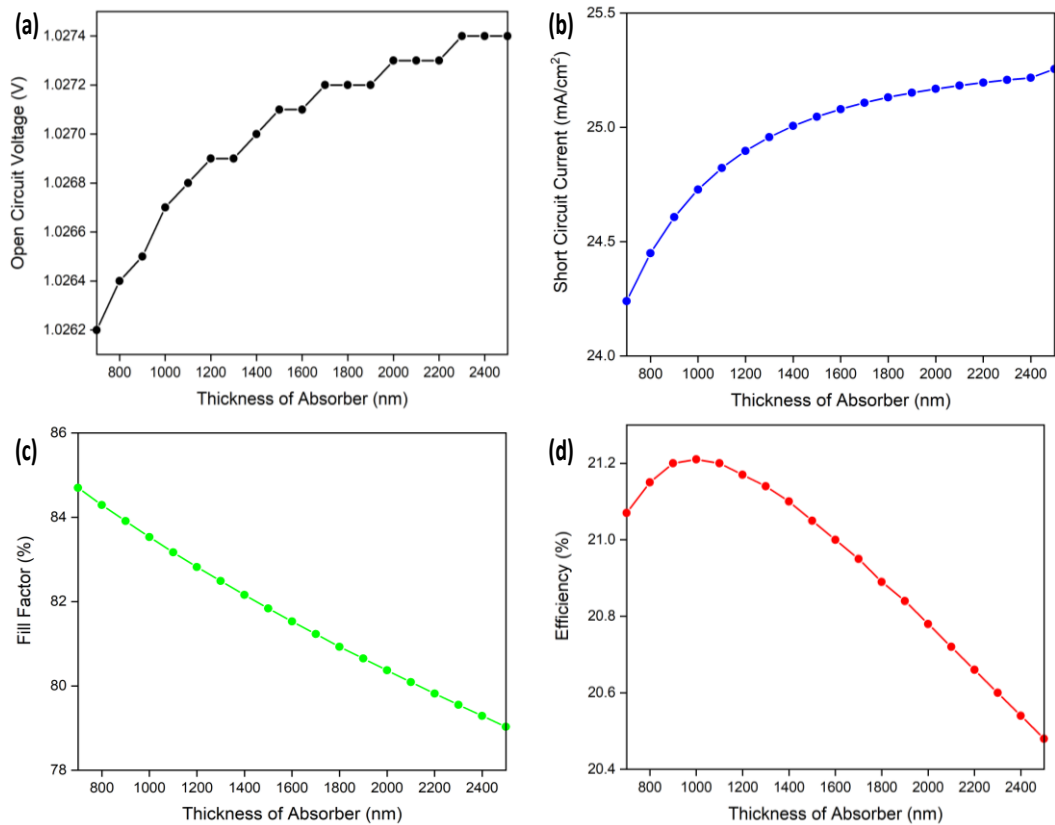


Fig. 3. Effect of the change in absorber thickness on (a) V_{OC} , (b) J_{SC} , (c) FF, and (d) PCE.

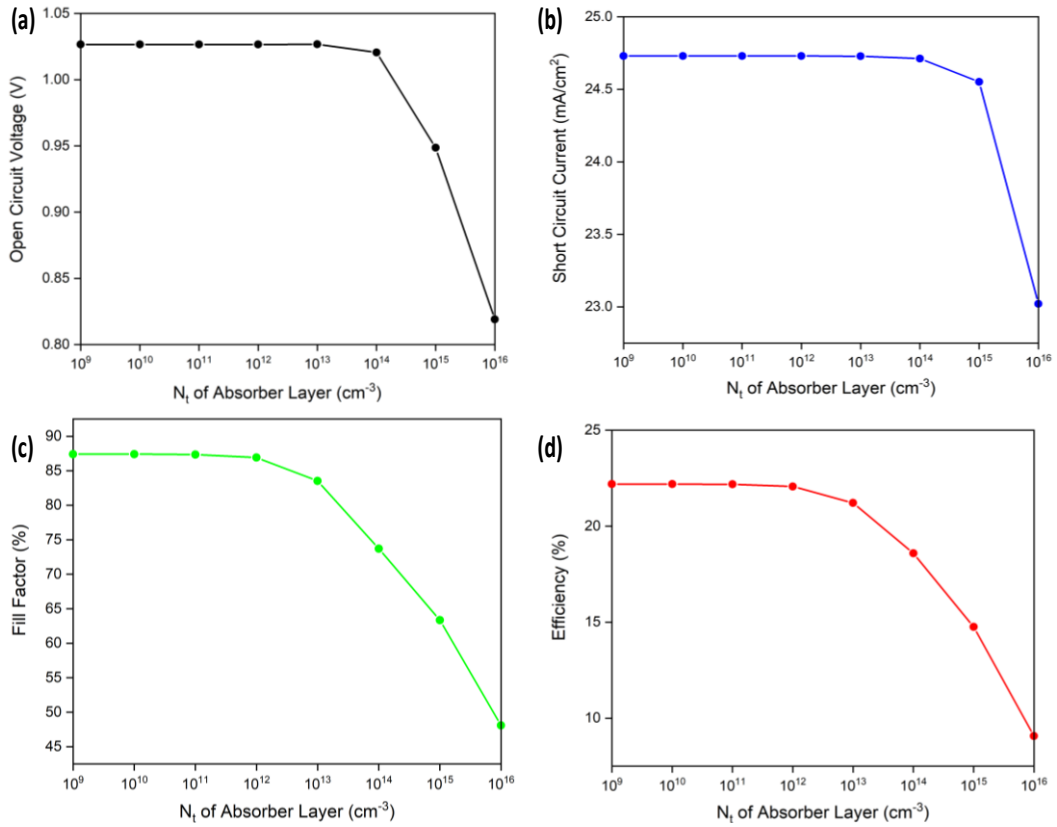


Fig. 4. Effect of the change in absorber layer defect density on (a) V_{OC} , (b) J_{SC} , (c) FF, and (d) PCE.

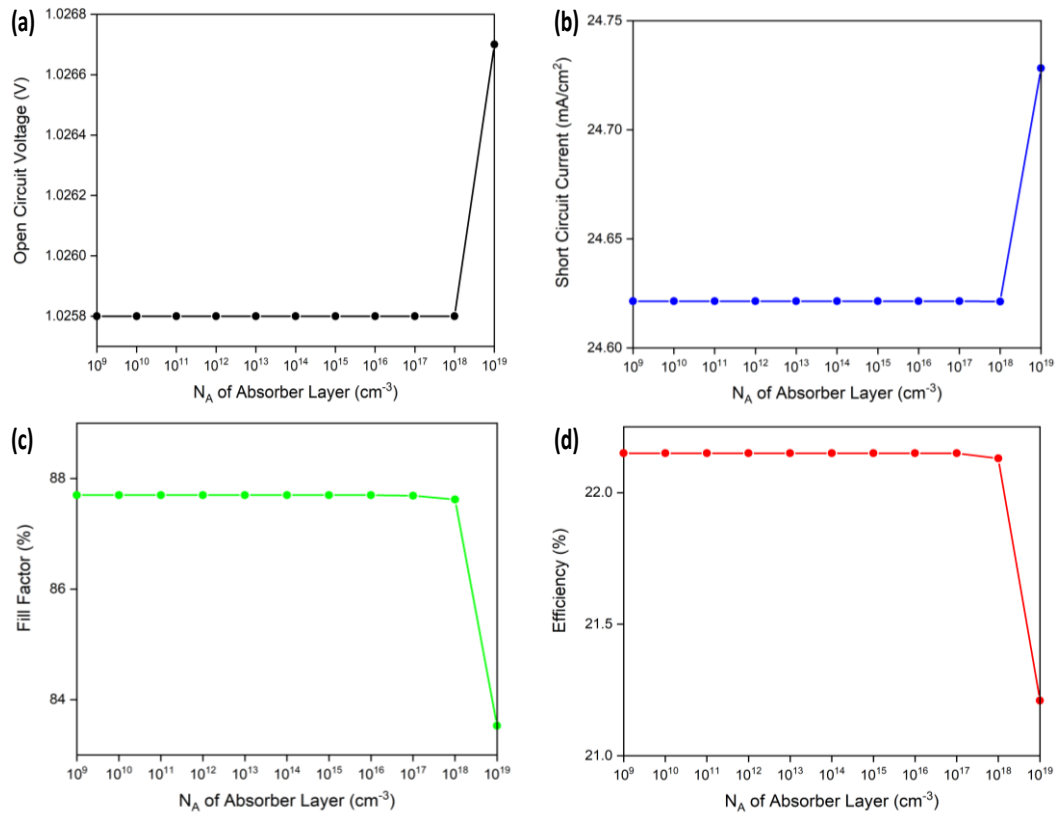


Fig. 5. Effect of the change in absorber doping density on (a) V_{OC} , (b) J_{SC} , (c) FF, and (d) PCE.

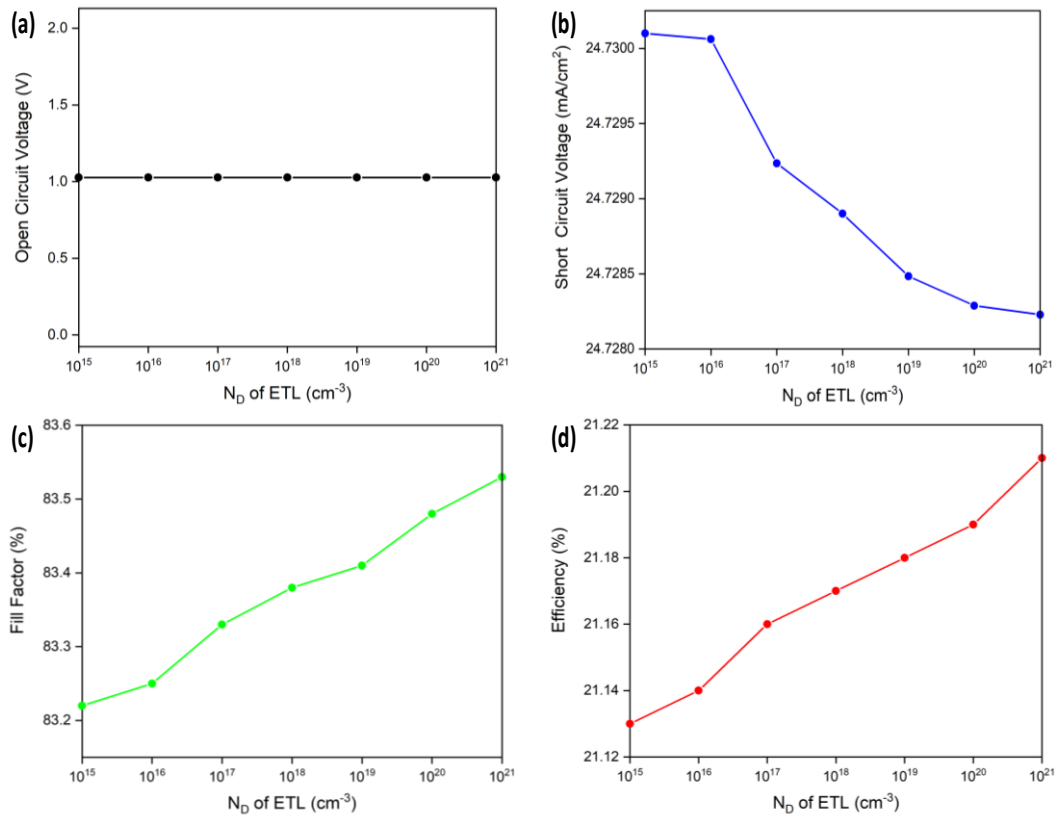


Fig. 6. Effect of the change in ETL doping density on (a) V_{OC} , (b) J_{SC} , (c) FF, and (d) PCE.

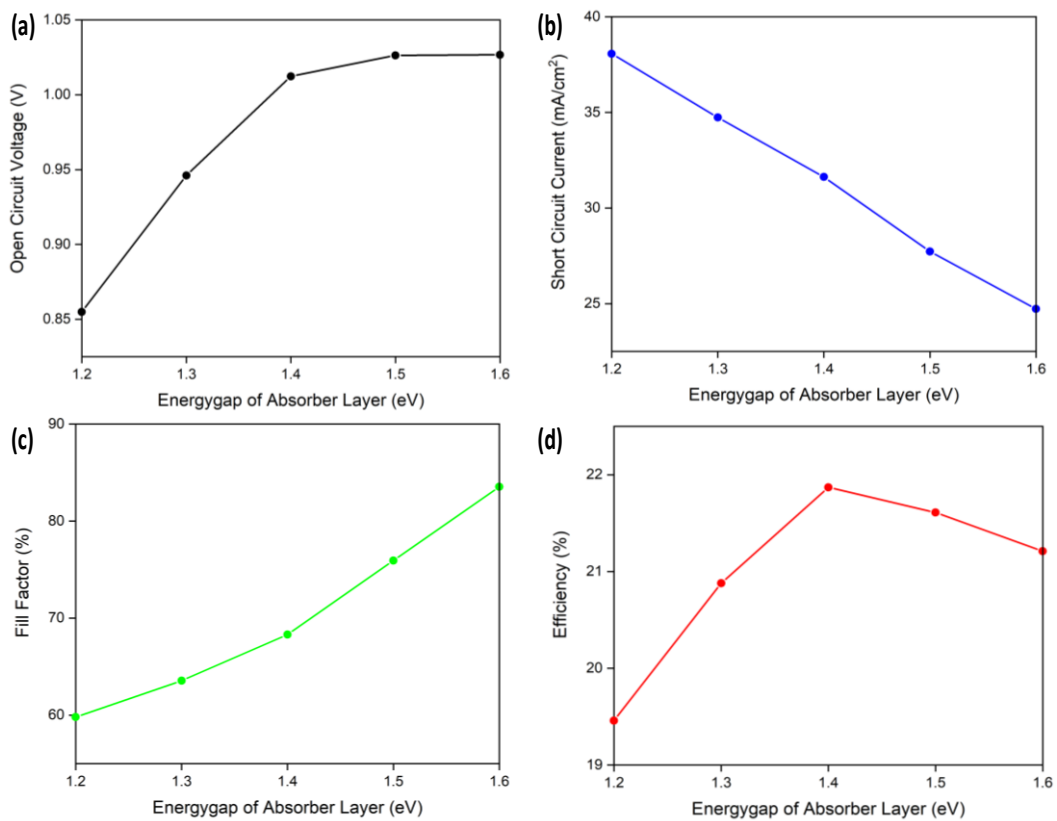


Fig. 7. Effect of the change in absorber layer energy gap on (a) V_{OC} , (b) J_{SC} , (c) FF, and (d) PCE.

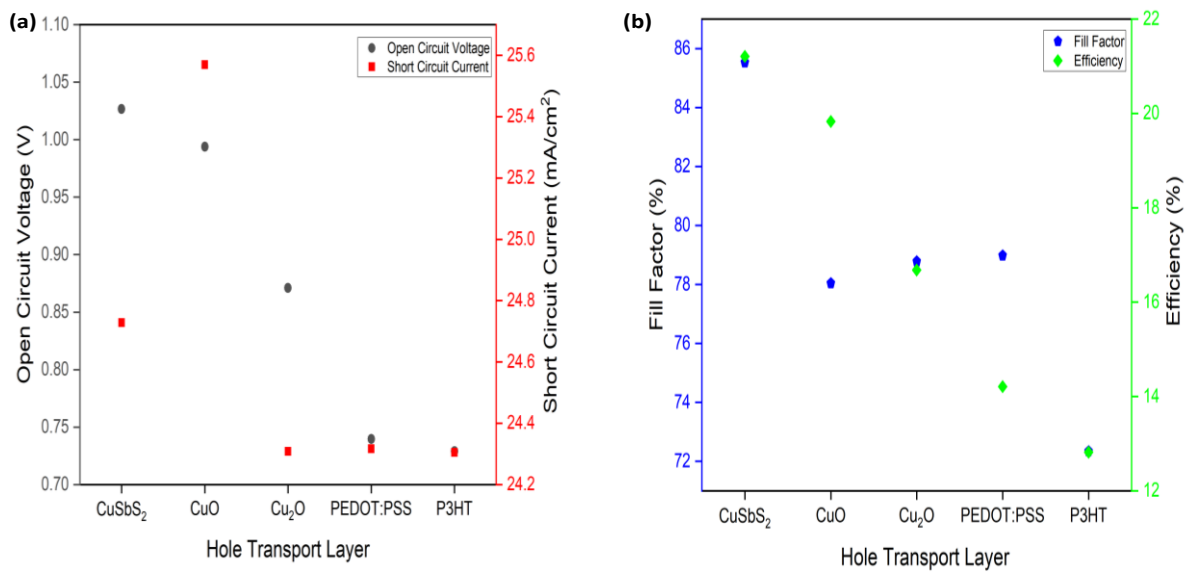


Fig. 8. Simulated (a) V_{OC} and J_{SC} , (b) FF and PCE values for different HTLs of the PSC.

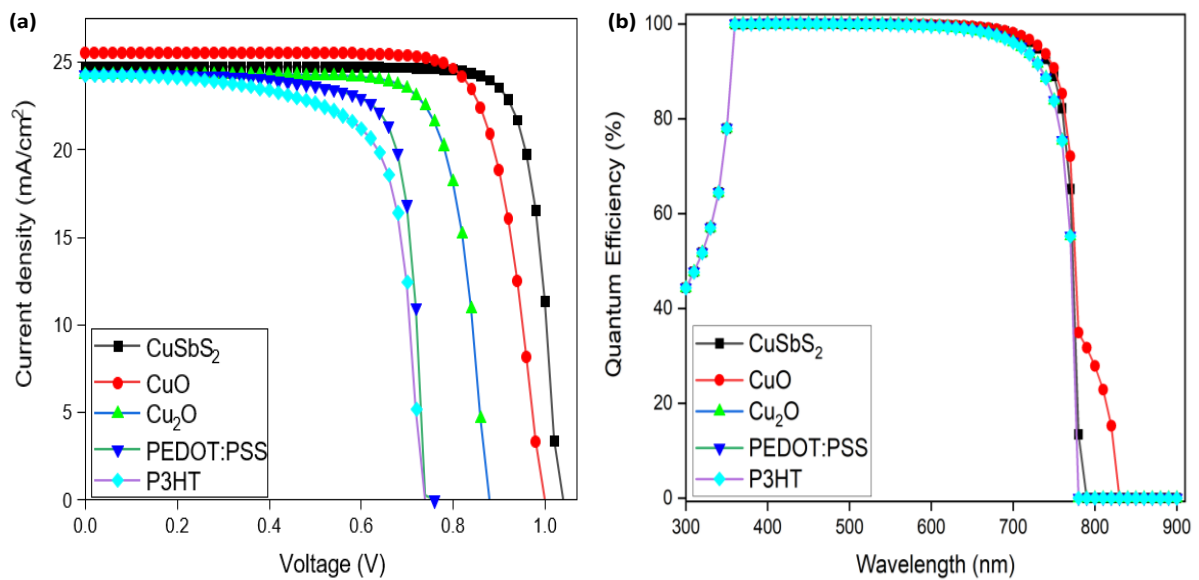


Fig. 9. Simulated (a) J-V and (b) QE curves for different HTLs of the PSC.

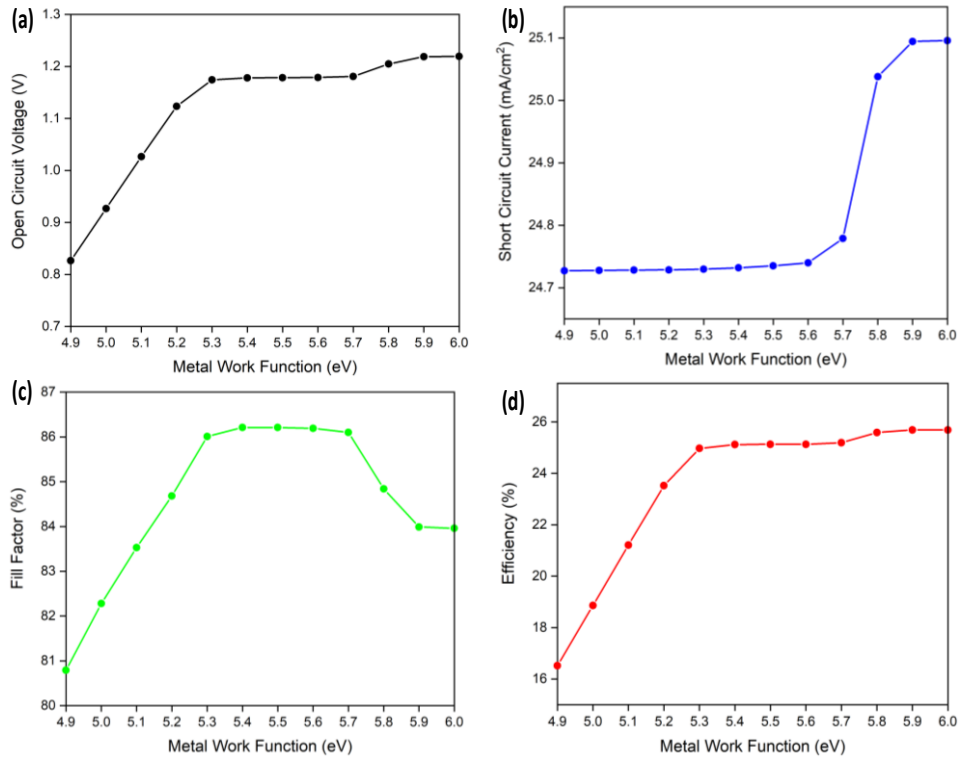


Fig. 10. Effect of the change in back contact work function on (a) V_{OC} , (b) J_{SC} , (c) FF, and (d) PCE.

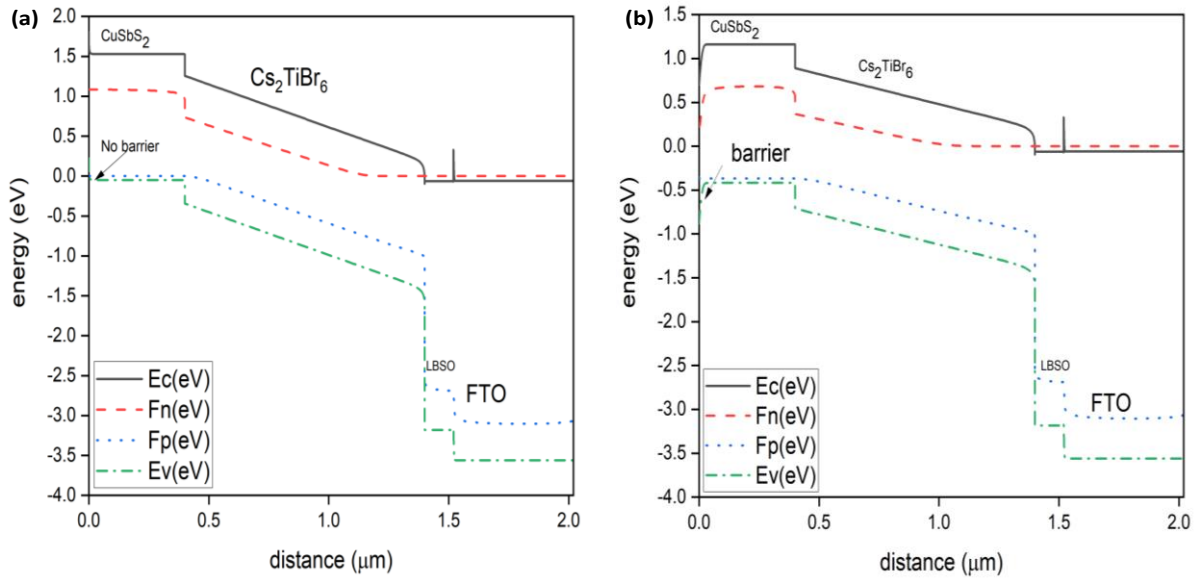


Fig. 11. Simulated energy band diagram for the metal work function of (a) 4.9 eV and (b) 6.0 eV.

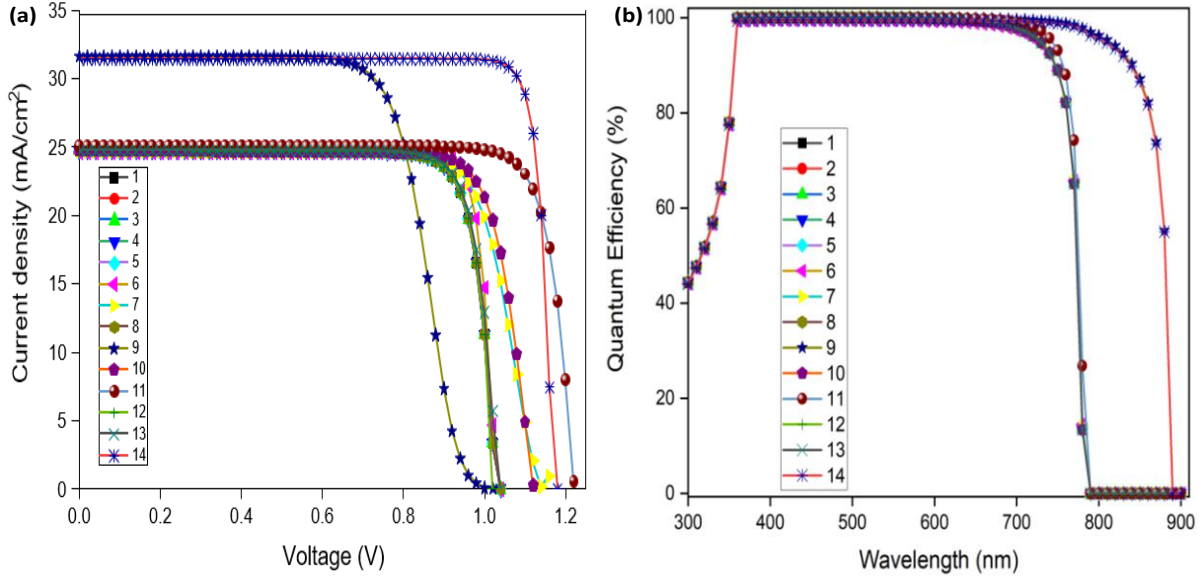


Fig. 12. Simulated optimized (a) J-V and (b) QE curves of the PSC (where the curve represents: **(1)** Initial parameters, **(2)** Optimized thickness of PAL, **(3)** Optimized thickness of ETL, **(4)** Optimized thickness of HTL, **(5)** Optimized N_t of the absorber, **(6)** Optimized N_A of the absorber, **(7)** Optimized N_A of HTL, **(8)** Optimized N_D of ETL, **(9)** Effect of E_g of the absorber, **(10)** Effect of χ_e of HTL, **(11)** Effect of ϕ of back contact, **(12)** Effect of temperature, **(13)** Effect of μ_h of HTL, and **(14)** Final optimization).

Table 1. Basic parameters for charge transport layers and absorbers.

Properties	Symbol	Unit	FTO	LBSO	Cs_2TiBr_6	CuSbS_2
thickness	W	nm	500	120	1000	400
bandgap	E_g	eV	3.5	3.12	1.6	1.58
electron affinity	χ	eV	4	4.4	4.47	4.2
dielectric permittivity (relative)	ϵ	-	9	22	10	14.6
CB effective density of states	N_c	cm^{-3}	2.2×10^{18}	1.8×10^{20}	6.0×10^{19}	2.0×10^{18}
VB effective density of states	N_v	cm^{-3}	1.8×10^{19}	1.8×10^{20}	2.14×10^{19}	1.0×10^{19}
electron thermal velocity	V_{thn}	cm/s	1×10^7	1×10^7	1×10^7	1×10^7
hole thermal velocity	V_{thp}	cm/s	1×10^7	1×10^7	1×10^7	1×10^7
electron mobility	μ_n	cm^2/Vs	20	0.69	4.4	49
hole mobility	μ_p	cm^2/Vs	10	0.69	2.5	49
shallow uniform donor density	N_D	cm^{-3}	2×10^{19}	2×10^{21}	1×10^{19}	0
shallow uniform acceptor density	N_A	cm^{-3}	0	0	1×10^{19}	1.38×10^{18}
references			[28]	[23], [51], [60], [61]	[9], [62]	[15]

Table 2. Defect parameters for charge transport layers and absorbers.

Parameters	Symbol	Unit	FTO	LBSO	Cs ₂ TiBr ₆	CuSbS ₂
defect type	-	-	Neutral	Neutral	Neutral	Neutral
capture cross section electrons	σ_n	cm ²	1×10^{-15}	1×10^{-15}	1×10^{-15}	1×10^{-15}
capture cross section holes	σ_p	cm ²	1×10^{-15}	1×10^{-15}	1×10^{-15}	1×10^{-15}
energetic distribution	-	-	Single	Single	Single	Single
reference for defect energy level E_t	-	-	Above E_v	Above E_v	Above E_v	Above E_v
energy level with respect of reference	-	eV	0.6	0.6	0.7	0.1
N_t total	N_t	cm ⁻³	1×10^{14}	1×10^{14}	1×10^{13}	1×10^{14}

Table 3. Defect parameters for interfacial contacts.

Parameters	Symbol	Unit	CuSbS ₂ /Cs ₂ TiBr ₆	Cs ₂ TiBr ₆ /LBSO
defect type	-	-	Neutral	Neutral
capture cross section electrons	σ_n	cm ²	1×10^{-19}	1×10^{-19}
capture cross section holes	σ_p	cm ²	1×10^{-19}	1×10^{-19}
energetic distribution	-	-	gauß	gauß
reference for defect energy level E_t	-	-	Above the highest EV	Above the highest EV
energy level w.r.t reference	-	eV	0.6	0.6
total density (integrated overall energies)	N_t	cm ⁻²	3.90×10^{10}	3.90×10^{10}
density at peak energy	-	eVcm ⁻²	2×10^{10}	2×10^{10}

Table 4. Basic parameters for different HTLs.

Properties	Unit	CuO [63]	Cu ₂ O [64]	PEDOT:PSS [10]	P3HT [55]
W	nm	400	400	400	400
E_g	eV	1.5	2.17	2.2	1.85
χ	eV	4.07	3.20	2.9	3.1
ϵ	-	18.1	7.11	3	3.4
N_c	cm ⁻³	2.0×10^{18}	2.0×10^{18}	2.0×10^{18}	2.0×10^{18}
N_v	cm ⁻³	1.0×10^{19}	1.0×10^{19}	1.0×10^{19}	1.0×10^{19}
V_{thn}	cm/s	1.0×10^7	1.0×10^7	1.0×10^7	1.0×10^7
V_{thp}	cm/s	1.0×10^7	1.0×10^7	1.0×10^7	1.0×10^7
μ_n	cm ² /V s	100	80	2.0×10^{-3}	1.0×10^{-4}
μ_p	cm ² /V s	0.1	80	2.0×10^{-3}	1.0×10^{-3}
N_D	cm ⁻³	0	0	0	0
N_A	cm ⁻³	1.38×10^{18}	1.38×10^{18}	1.38×10^{18}	1.38×10^{18}

Table 5. Effect of $E_{C_ETL}-E_{V_HTL}$, $\phi_{BC} - E_{C_ETL}$, qV_{bi} , and photovoltaic parameters on the PSC.

HTL	μ_p [cm ² /Vs]	E_g [eV]	$E_{C_ETL}-E_{V_HTL}$ [eV]	$\phi_{BC} - E_{C_ETL}$ [eV]	qV_{bi} [eV]	V_{oc} [eV]	J_{sc} [mA/cm ²]	FF [%]	PCE [%]
CuSbS ₂	49	1.58	1.38	0.70	0.91	1.0267	24.728208	85.53	21.21
CuO	0.1	1.50	1.17	0.70	0.81	0.9939	25.569850	78.04	19.83
Cu ₂ O	80	2.17	0.97	0.70	0.70	0.8711	24.308312	78.78	16.68
PEDOT:PSS	2.0×10^{-3}	2.20	0.70	0.70	0.48	0.7397	24.316510	78.98	14.21
P3HT	1.0×10^{-3}	1.85	0.55	0.70	0.29	0.7290	24.304812	72.34	12.82

Table 6. Performance comparison of existing Cs₂TiBr₆ and MAPbI₃-based PSCs.

Structure	PCE [%]	V _{oc} [V]	J _{sc} (mA/cm ²)	FF [%]	References
FTO/TiO ₂ /Cs ₂ TiBr ₆ /NiO/Au	8.51	1.12	10.25	73.59	[65]
FTO/SnO ₂ /Cs ₂ TiBr ₆ /MoO ₃ /Au	11.49	1.53	8.66	86.45	[66]
FTO/V ₂ O ₅ /Cs ₂ TiBr ₆ /CdTe/Au	14.55	0.92	18.176	86.58	[67]
FTO/ZnO/Cs ₂ TiBr ₆ /Cu ₂ O/Au	18.15	1.53	13.60	87.23	[45]
FTO/TiO ₂ /MAPbI ₃ /PTAA/Au	19.6	1.07	23.3	78.6	[23]
FTO/LBSO/MAPbI ₃ /PTAA/Au	21.3	1.12	23.4	81.3	[23]
FTO/LBSO/Cs ₂ TiBr ₆ /CuSbS ₂ /Se	29.13	1.11	29.60	88.58	This Work

Supplementary File

Computational equations used in SCAPS:

The Poisson's equation (equation 1), the electron continuity equation (equation 2), and the hole continuity equation (equation 3) are given below [1]:

$$\frac{d}{dx} \left(-\varepsilon(x) \frac{d\psi}{dx} \right) = q [p(x) - n(x) + N_d^+(x) - N_a^-(x)] \dots \dots \dots (1)$$

$$\frac{\partial j_n}{\partial x} = q (R_n - G + \frac{\partial n}{\partial t}) \dots \dots \dots (2)$$

$$\frac{\partial j_p}{\partial x} = -q (R_p - G + \frac{\partial p}{\partial t}) \dots \dots \dots (3)$$

Where, ε is the permittivity, q is the electron charge, ψ is the electrostatic potential, n is the total electron density, p is the total hole density, N_d^+ is the ionized donor-like doping concentration, N_a^- is the ionized acceptor-like doping concentration, j_n and j_p are the electron and hole current densities respectively, R_n and R_p are the net recombination rates for electron and hole per unit volume respectively, and G is the generation rate per unit volume.

Computational equations utilized in wxAMPS:

In 1-D space, Poisson's equation is given by [2]:

$$\frac{d}{dx} \left(-\varepsilon(x) \frac{d\psi'}{dx} \right) = q \cdot [p(x) - n(x) + N_D^+(x) - N_A^-(x) + pt(x) - nt(x)] \dots \dots \dots (4)$$

Where, the electrostatic potential ψ' and the free electron n , free hole p , trapped electron n_t , and trapped hole p_t as well as the ionized donor-like doping N_D^+ and ionized acceptor-like doping N_A^- concentrations are all functions of the position coordinate x . The continuity equation for the free electrons in the delocalized states of the conduction band has the form [3]:

$$\frac{1}{q} \left(\frac{dJ_n}{dx} \right) = -G_{op}(x) + R(x) \dots \dots \dots (5)$$

Again, the continuity equation for the free holes in the delocalized states of the valence band has the form:

$$\frac{1}{q} \left(\frac{dJ_p}{dx} \right) = G_{op}(x) - R(x) \dots \dots \dots (6)$$

Where, J_n and J_p are, respectively, the electron and hole current densities. The term $R(x)$ is the net recombination rate resulting from band-to-band (direct) recombination and SRH (indirect)

recombination traffic through gap states. The net direct recombination rate is [4]:

$$R_D(x) = \beta(np - n_i^2) \dots \dots \dots (7)$$

Where, β is a proportionality constant, which depends on the material's energy band structure under analysis, and n and p are the band carrier concentrations present when devices are subjected to a voltage bias, light bias, or both. The continuity equations include the term $G_{op}(x)$, which is the optical generation rate as a function of x due to externally imposed illumination.

Absorption data for the perovskite solar cell:

Absorption data for each layer was achieved from the new Eg-sqrt model (SCAPS version 3.3.07), which is the updated model of the traditional SCAPS model (traditional sqrt $(h\nu - E_g)$)

law model) and can be found from the "Tauc laws". The updated Eg-sqrt model follows equation 8 [5].

$$\alpha(h\nu) = (\alpha_0 + \beta_0 \frac{E_g}{h\nu}) \sqrt{\frac{h\nu}{E_g} - 1} \dots \dots \dots (8)$$

Where, α is the optical absorption constant, $h\nu$ is the photon energy, and E_g is the bandgap. The model constants α_0 and β_0 have the dimension of absorption constant (e.g., 1/cm) and are related to the traditional model constants A and B by the relations:

$$\alpha_0 = A\sqrt{E_g} \text{ and } \beta_0 = \frac{B}{\sqrt{E_g}}$$

SRH recombination due to the defects in the perovskite layer:

The charge carriers in the PSC are recombined by Shockley-Read-Hall (SRH) recombination process and the net recombination rate (R^{SRH}) for SRH recombination is given by the following equation [1]:

$$R^{SRH} = \frac{v\sigma_n\sigma_p N_T [np - n_i^2]}{\sigma_p[p + p_1] + \sigma_n[n + n_1]} \dots \dots \dots (9)$$

Where, σ_n and σ_p are the capture cross-sections for electrons and holes, v is the electron thermal velocity, N_T is the atomistic defect concentration, n_i is the intrinsic carrier density, n and p are the concentrations of electron and hole at equilibrium, and n_1 and p_1 are the concentrations of electrons and holes in trap defect and valence band, respectively.

According to equation 9, the R^{SRH} is directly proportional to the defect density in the perovskite absorber layer. Again, the R^{SRH} has an impact on the carrier diffusion length. The diffusion length increases with decreasing the perovskite absorber layer's defect density, which improves the solar cell performance. The relation between the diffusion length, carrier mobility, and lifetime at a temperature T is expressed in equation 10 [4].

$$L_D = \sqrt{\frac{\mu_{(e,h)R}SRHT}{q}} \times \tau_{lifetime} \dots \dots \dots (10)$$

Where, L_D , $\mu_{(e,h)}$, and $\tau_{lifetime}$ are the diffusion length, the electron and hole mobility, and the minority-carrier lifetime, respectively. Moreover, $\tau_{lifetime}$ depends upon the defect density and capture cross-section area for electrons and holes. The relation between $\tau_{lifetime}$ and bulk defect density is expressed in equation 11.

$$\tau_{lifetime} = \frac{1}{N_T \delta v_{th}} \dots \dots \dots (11)$$

Here, δ , v_{th} , and N_T represent the capture cross-section area for electrons and holes, the thermal velocity of carriers, and defect concentration, respectively.

Validation of the model using wxAMPS:

The simulations were carried out using wxAMPS (version 2.0) for validating the results attained from the SCAPS software. The simulations were run at 1000 nm absorber thickness in both software to find the variations in V_{oc} , J_{sc} , FF, and PCE of the PSC. All the simulations were performed at 300 K working temperature and AM1.5G solar spectrum. Table S1 shows the comparison in the photovoltaic performance between the two simulation tools. Furthermore, Fig. S1(a) and Fig. S1(b) exhibit the comparison in the J-V and QE curves, respectively, between the two simulation tools.

Table S1. Comparison between the SCAPS and wxAMPS results at 1000 nm absorber thickness of the PSC.

Serial	Software	V_{oc}	J_{sc}	FF	PCE
		V	mA/cm ²	%	%
1	SCAPS	1.0267	24.7282	83.53	21.21
2	wxAMPS	1.0165	23.8396	88.88	21.53

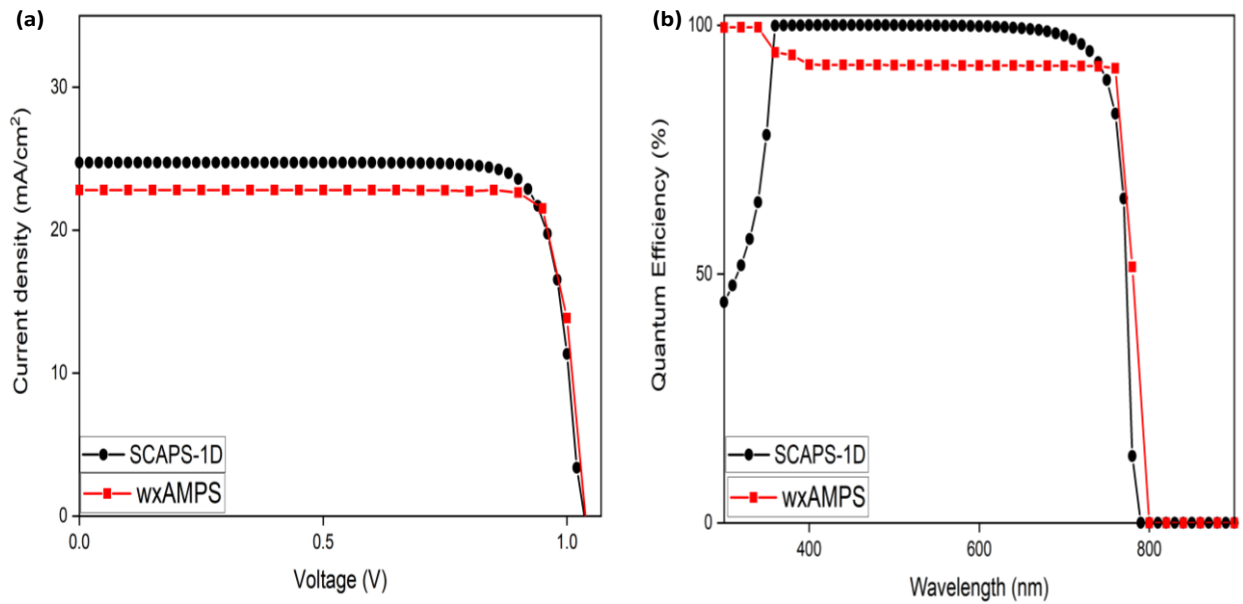


Fig. S1. Comparison in the (a) J-V and (b) QE curves of the PSC between the wxAMPS and SCAPS software at 1000 nm absorber thickness.

SCAPS simulation working procedure:

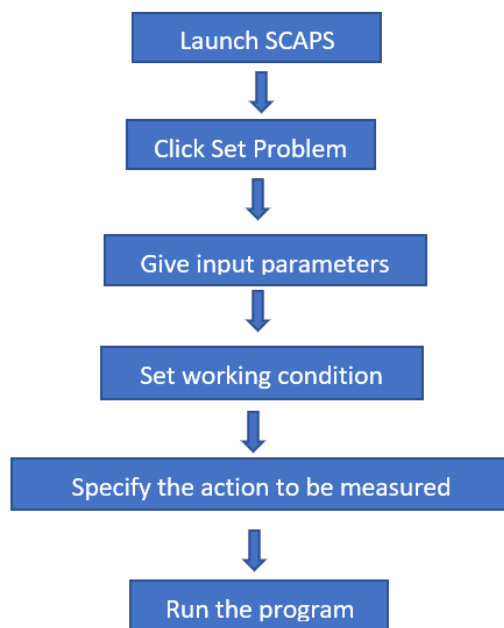


Fig. S2. SCAPS simulation working process [6].

Results and Discussion:

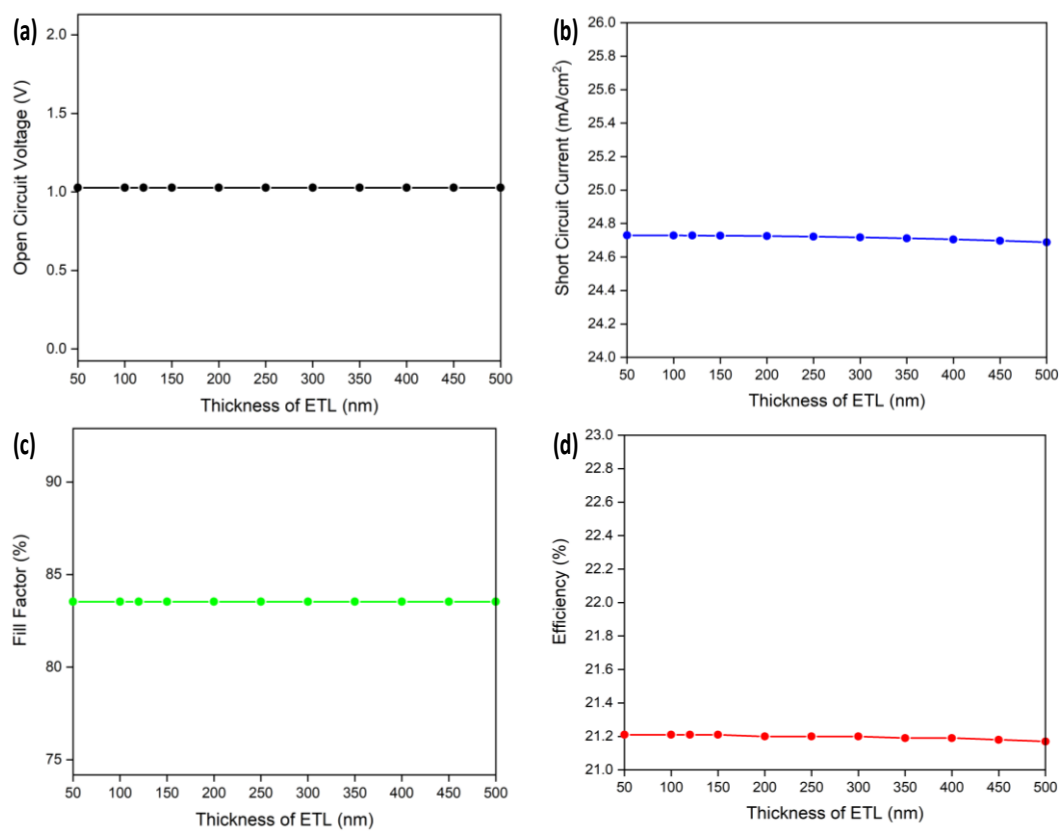


Fig. S3. Effect of the change in ETL thickness on (a) V_{oc} , (b) J_{sc} , (c) FF, and (d) PCE.

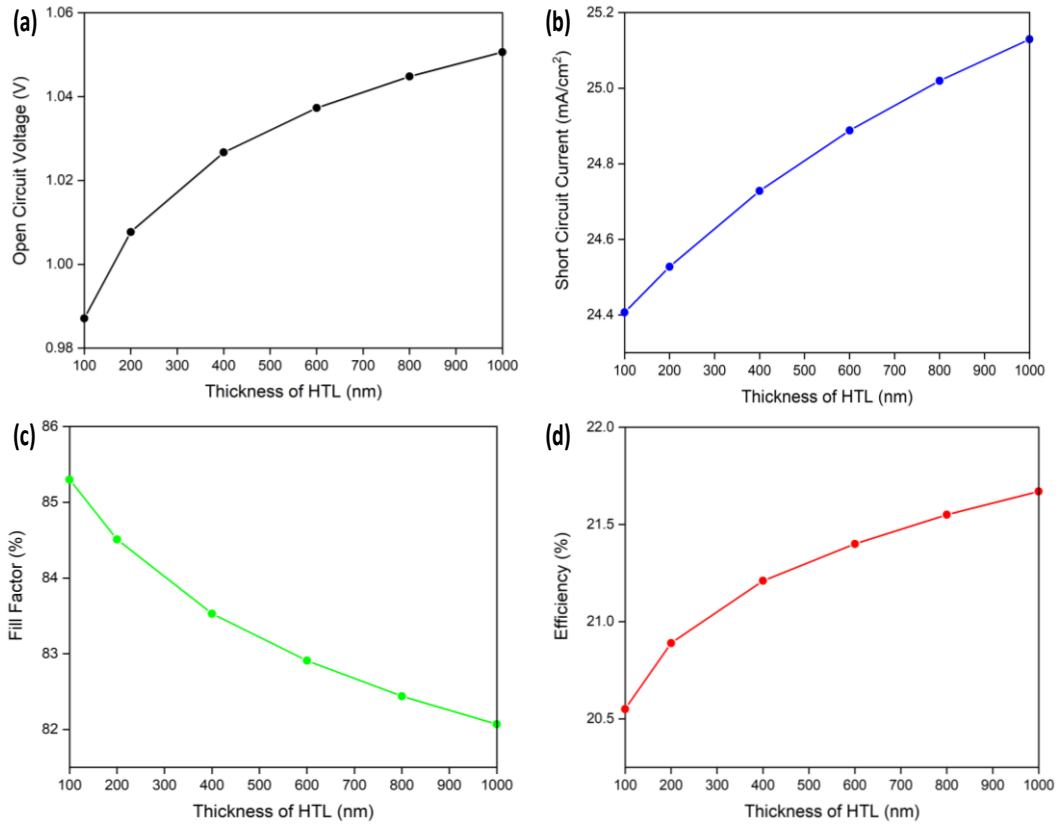


Fig. S4. Effect of the change in HTL thickness on (a) V_{OC} , (b) J_{SC} , (c) FF, and (d) PCE.

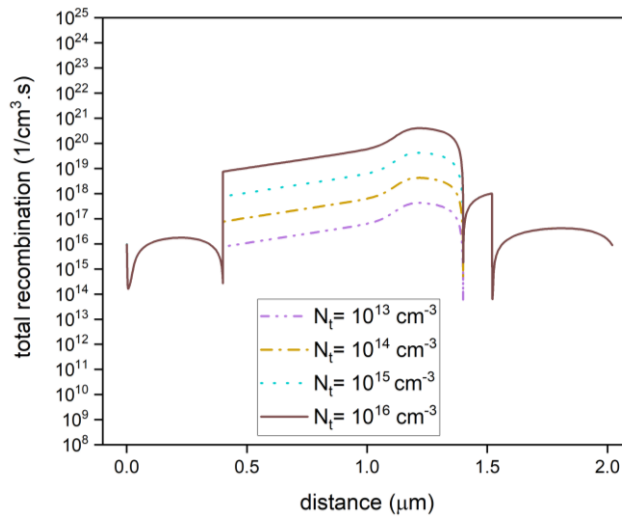


Fig. S5. Total recombination profile of absorber layer at different absorber defect densities.

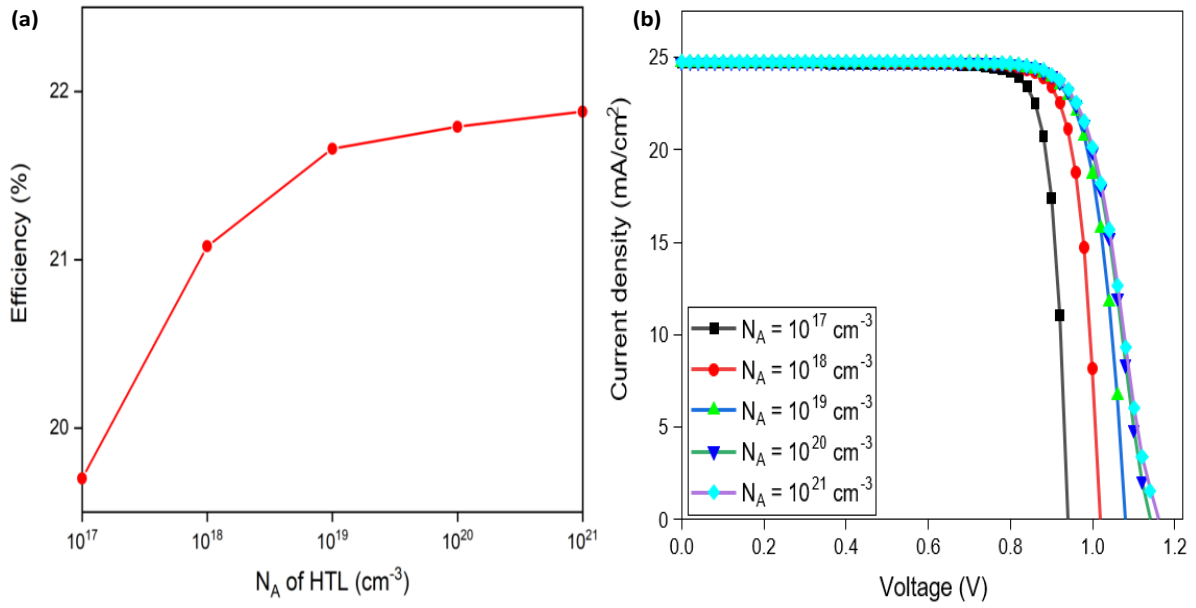


Fig. S6. Effect of the change in HTL doping density on **(a)** PCE and **(b)** J-V curves.

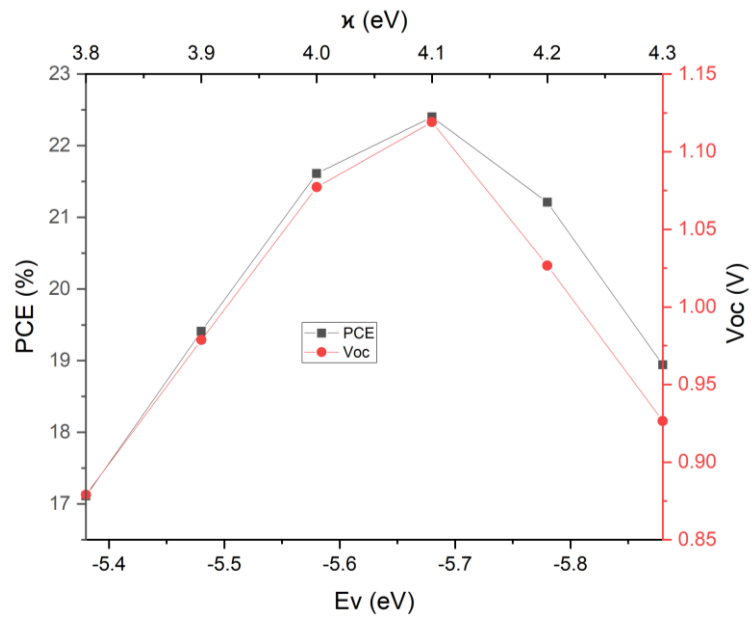


Fig. S7. Influence of the electron affinity of CuSbS_2 on the performance of the PSC.

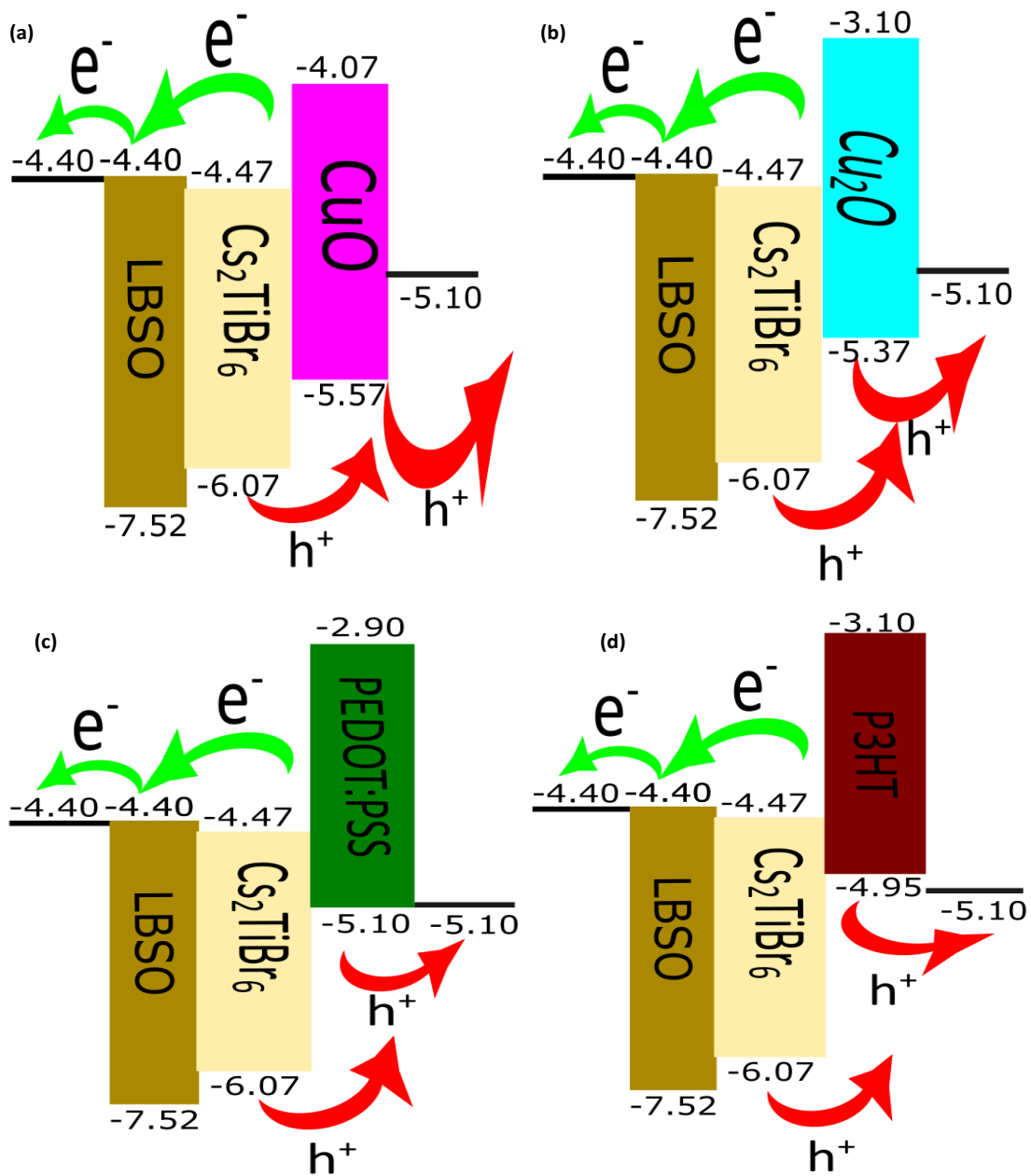


Fig. S8. Energy band alignment diagram for various HTLs of the PSC; **(a)** CuO, **(b)** Cu_2O , **(c)** PEDOT:PSS, and **(d)** P3HT.

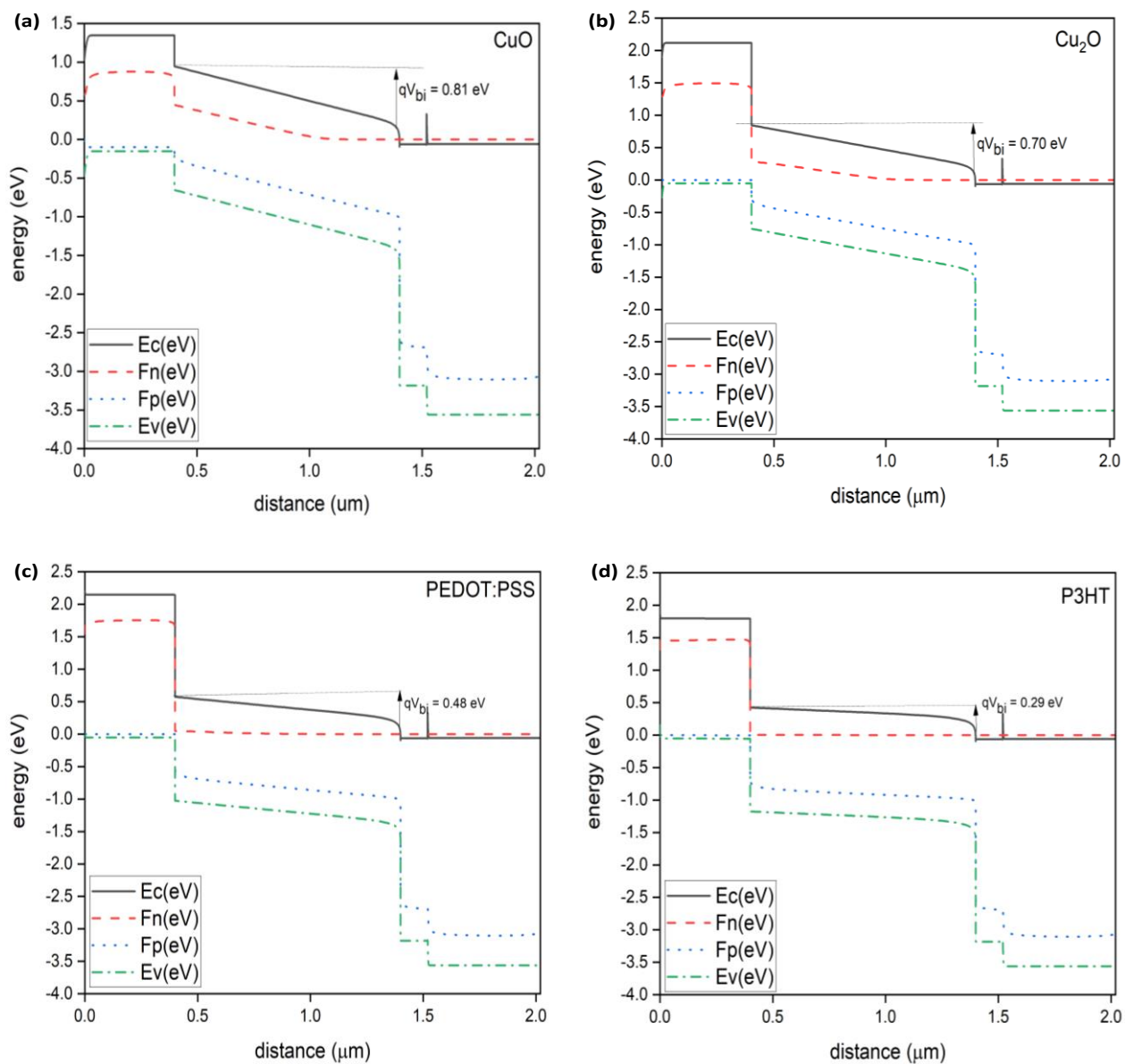


Fig. S9. Energy band diagram for various HTLs of the PSC; **(a)** CuO, **(b)** Cu_2O , **(c)** PEDOT:PSS, and **(d)** P3HT.

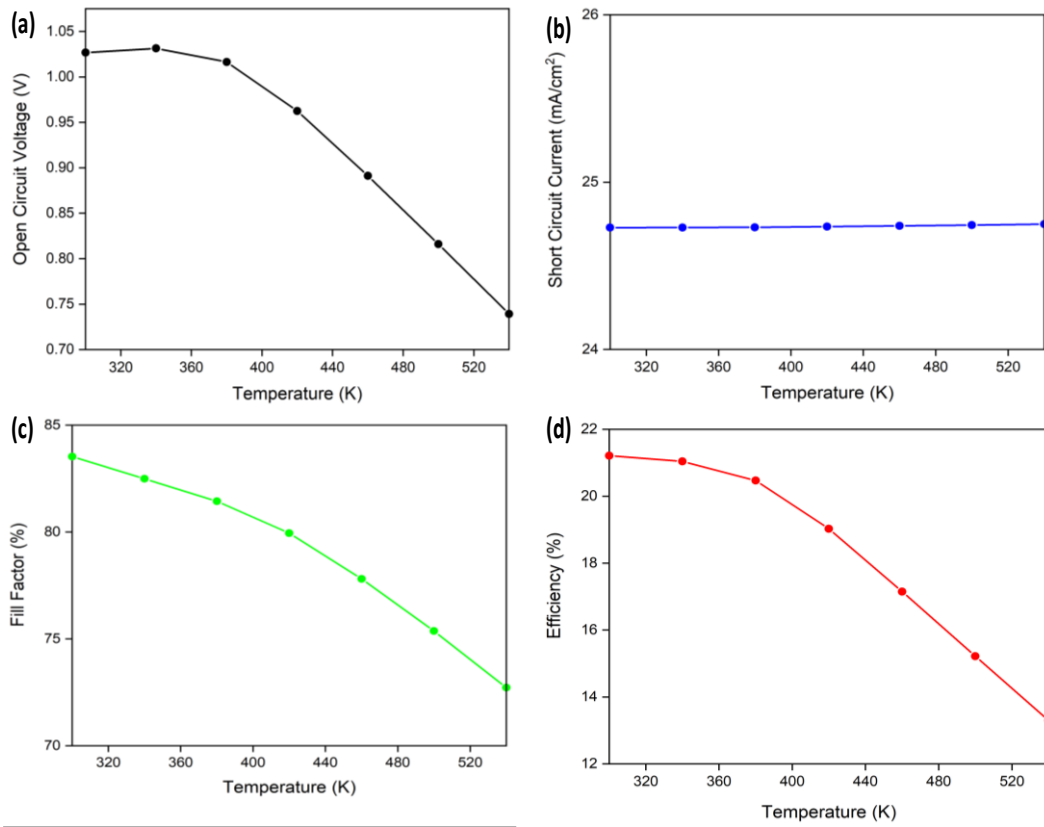


Fig. S10. Effect of the change in temperature on (a) V_{OC} , (b) J_{SC} , (c) FF, and (d) PCE.

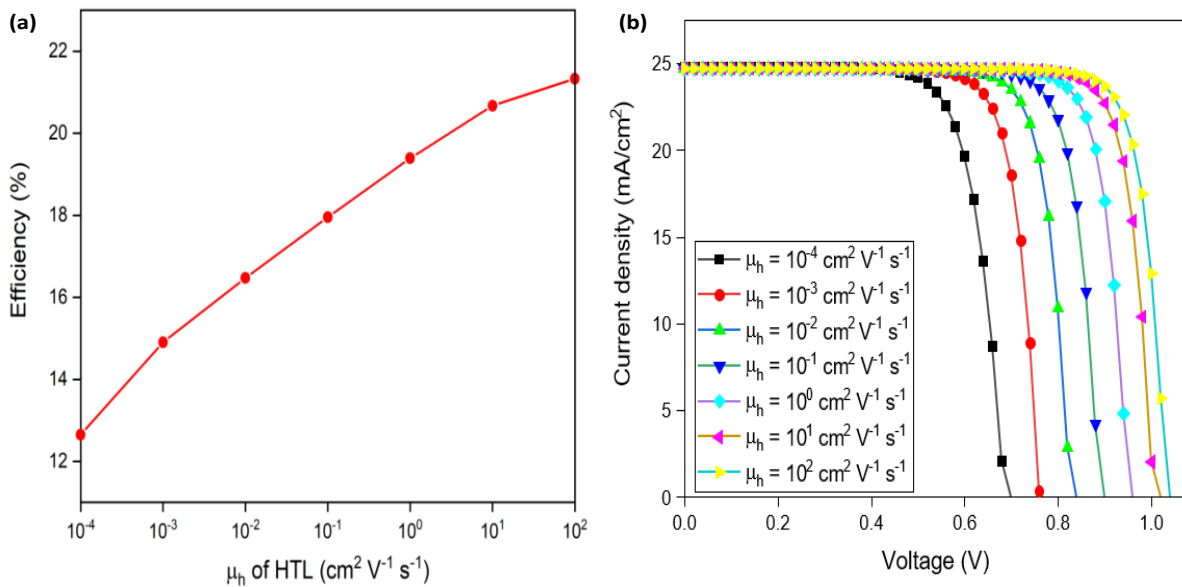


Fig. S11. Effect of the change in hole mobility of HTL on the (a) PCE and (b) J-V curves.

References:

- [1] M. T. Islam *et al.*, "Numerical simulation studies of Cs₃Bi₂I₉ perovskite solar device with optimal selection of electron and hole transport layers," *Optik (Stuttg.)*, vol. 231, no. January, p. 166417, 2021, doi: 10.1016/j.ijleo.2021.166417.
- [2] I. Alam and M. A. Ashraf, "Effect of different device parameters on tin-based perovskite solar cell coupled with In₂S₃ electron transport layer and CuSCN and Spiro-OMeTAD alternative hole transport layers for high-efficiency performance," *Energy Sources, Part A Recover. Util. Environ. Eff.*, vol. 2020, 2020, doi: 10.1080/15567036.2020.1820628.
- [3] M. T. Islam *et al.*, "Numerical simulation studies of a fully inorganic Cs₂AgBiBr₆ perovskite solar device," *Opt. Mater. (Amst.)*, vol. 105, no. March, p. 109957, 2020, doi: 10.1016/j.optmat.2020.109957.
- [4] I. Alam, R. Mollick, and M. A. Ashraf, "Numerical simulation of Cs₂AgBiBr₆-based perovskite solar cell with ZnO nanorod and P3HT as the charge transport layers," *Phys. B Condens. Matter*, vol. 618, no. June, p. 413187, 2021, doi: 10.1016/j.physb.2021.413187.
- [5] M. Burgelman, "Models for the optical absorption of materials in SCAPS," pp. 1-13, 2018, <https://scaps.elis.ugent.be/SCAPS%20manual%20most%20recent.pdf>.
- [6] A. Slami, M. Bouchaour, and L. Merad, "Numerical Study of Based Perovskite Solar Cells by SCAPS-1D," *Int. J. Energy Environ.*, vol. 13, pp. 17–21, 2019.